Nano Research Energy

ISSN 2791-0091 CN 10-1944/O6
https://doi.org/10.26599/NRE.2026.9120292

Research Article

Oxide-side lanthanum regulation enables trap-to-relay conversion of hydrogen spillover at MoO_2/Ni_4Mo interfaces

Kejun Yan[1,2], Jiahui Luo[1,2], Baoxin Wu[2,3], Yongbiao Mu[1,2], Zhiqing Tang[1,2], Yu Xu[1,2], Lei Wei[1,2], Lin Zeng[1,2](✉)

[1] Shenzhen Key Laboratory of Hydrogen Energy, Department of Mechanical and Energy Engineering, Southern University of Science and Technology, Shenzhen 518055, China

[2] SUSTech Energy Institute for Carbon Neutrality, Southern University of Science and Technology, Shenzhen 518055, China

[3] Department of Mechanical Engineering, The Hong Kong Polytechnic University, Hung Hom, Kowloon, Hong Kong, China

Nano Research Energy, **Just Accepted Manuscript** • https://doi.org/10.26599/NRE.2026.9120292

https://www.sciopen.com/journal/2791-0091 on Nov. 18, 2026

© The Authors(s)

Just Accepted

This is a "Just Accepted" manuscript, which has been examined by the peer-review process and has been accepted for publication. A "Just Accepted" manuscript is published online shortly after its acceptance, which is prior to technical editing and formatting and author proofing. Tsinghua University Press (TUP) provides "Just Accepted" as an optional and free service which allows authors to make their results available to the research community as soon as possible after acceptance. After a manuscript has been technically edited and formatted, and the page proofs have been corrected, it will be removed from the "Just Accepted" web site and published officially with volume and article number (e.g., Nano Research Energy, 2025, 4, e9120191). Please note that technical editing may introduce minor changes to the manuscript text and/or graphics which may affect the content, and all legal disclaimers that apply to the journal pertain. In no event shall TUP be held responsible for errors or consequences arising from the use of any information contained in these "Just Accepted" manuscripts. To cite this manuscript please use its Digital Object Identifier (DOI®), which is identical for all formats of publication.

Just Accepted

ISSN 2791-0091 (print); 2790-8119 (online)
https://doi.org/10.26599/NRE.2026.9120292
Research Article

TABLE OF CONTENTS (TOC)

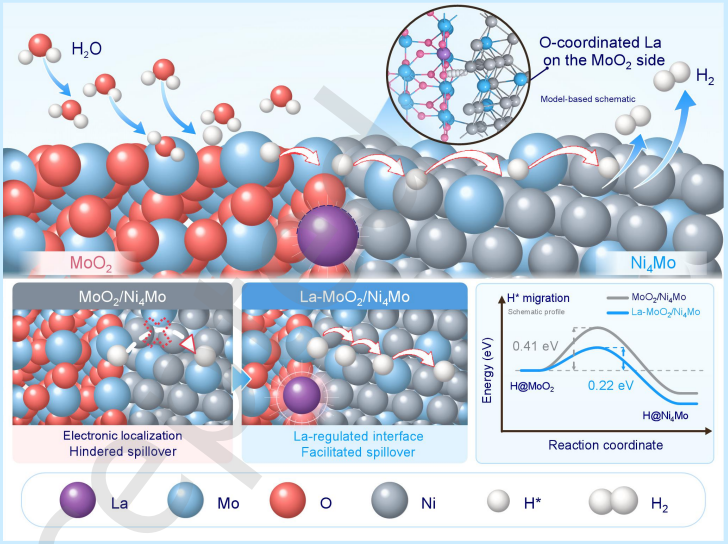
Oxide-side lanthanum regulation enables trap-to-relay conversion of hydrogen spillover at MoO_2/Ni_4Mo interfaces

Kejun Yan[a,b], Jiahui Luo[a,b], Baoxin Wu[b,c], Yongbiao Mu[a,b], Zhiqing Tang[a,b], Yu Xu[a,b], Lei Wei[a,b], Lin Zeng[a,b*]

[a] Shenzhen Key Laboratory of Hydrogen Energy, Department of Mechanical and Energy Engineering, Southern University of Science and Technology, Shenzhen 518055, China.

[b] SUSTech Energy Institute for Carbon Neutrality, Southern University of Science and Technology, Shenzhen 518055, China.

[c] Department of Mechanical Engineering, The Hong Kong Polytechnic University, Hung Hom, Kowloon, Hong Kong SAR, China.



Lanthanum regulation on the MoO_2 side converts interfacial H* trapping into continuous hydrogen relay, lowers the migration barrier, and thereby enhances HER activity.

Lin Zeng, zengl3@sustech.edu.cn

Just Accepted

ISSN 2791-0091 (print); 2790-8119 (online)
https://doi.org/10.26599/NRE.2026.9120292
Research Article

Oxide-side lanthanum regulation enables trap-to-relay conversion of hydrogen spillover at MoO_2/Ni_4Mo interfaces

Kejun Yan[1,2], Jiahui Luo[1,2], Baoxin Wu[2,3], Yongbiao Mu[1,2], Zhiqing Tang[1,2], Yu Xu[1,2], Lei Wei[1,2], and Lin Zeng[1,2] (✉)

[1]*Shenzhen Key Laboratory of Hydrogen Energy, Department of Mechanical and Energy Engineering, Southern University of Science and Technology, Shenzhen 518055, China*
[2]*SUSTech Energy Institute for Carbon Neutrality, Southern University of Science and Technology, Shenzhen 518055, China*
[3]*Department of Mechanical Engineering, The Hong Kong Polytechnic University, Hung Hom, Kowloon, Hong Kong, China*

© The Author(s) 2026

Received: 8 October 2026 / **Revised:** 22 September 2026 / **Accepted:** 2 November 2026

ABSTRACT

Efficient alkaline hydrogen evolution requires not only rapid water dissociation but also continuous interfacial transport and consumption of hydrogen intermediates. However, alloy/oxide heterointerfaces designed to couple these elementary steps often suffer from electronic mismatch, leading to localized hydrogen intermediates (H*) trapping and interrupted hydrogen spillover. Here, an oxide-side lanthanum-regulated MoO_2/Ni_4Mo heterostructure is developed to convert the interfacial H* bridge from an electronic trap into a relay-permissive junction. La is preferentially accommodated in the oxygen-coordinated MoO_2-side environment, where it attenuates local contact-potential mismatch, redistributes near-Fermi interfacial states, and strengthens alloy/oxide coupling without forming a dominant La-centered hydrogen-evolution site. This electronic reconfiguration enables a continuous MoO_2-to-Ni_4Mo hydrogen-relay pathway by lowering the interfacial H* migration barrier while maintaining favorable water-activation and H_2-release energetics. Consequently, La-MoO_2/Ni_4Mo delivers an overpotential of 14 mV at 10 mA cm^{-2} and a Tafel slope of 31.9 mV dec^{-1} in alkaline electrolyte. When implemented as a cathode in an anion-exchange-membrane water electrolyzer (AEMWE), it achieves 1 A cm^{-2} at 1.74 V and sustains stable operation for 1000 h at 70 ℃. This work establishes oxide-side lanthanum-mediated interfacial electronic regulation as an effective strategy for constructing spillover-active hydrogen-evolution electrodes for practical alkaline water electrolysis.

KEYWORDS

alkaline water electrolysis, hydrogen evolution reaction, hydrogen spillover, alloy/oxide heterointerfaces, rare earth

1 Introduction

Green hydrogen production by water electrolysis is a central technology for coupling renewable electricity with carbon-neutral fuel and chemical manufacturing[1-2]. Among emerging electrolyzer technologies, the anion-exchange-membrane water electrolyzer (AEMWE) is particularly attractive because it combines the compact membrane-electrode configuration of proton-exchange-membrane systems with the possibility of using earth-abundant catalysts in alkaline media[3-6]. However, the cathodic hydrogen evolution reaction (HER) in alkaline electrolytes remains kinetically more complicated than that in acidic environments. In acidic HER[7], adsorbed hydrogen intermediates can be generated directly from proton discharge, whereas alkaline HER requires the prior activation and dissociation of water molecules before hydrogen intermediates (H*) formation[8-9]. This additional water-dissociation step makes the overall reaction strongly dependent on the kinetic coupling among water activation, H* adsorption, interfacial hydrogen transfer, and H_2 release.[10] Therefore, developing efficient non-precious HER electrodes for practical AEMWE requires catalytic interfaces that can sustain a continuous hydrogen-relay sequence rather than merely optimizing the adsorption energy of H* at isolated active sites[11].

Heterogeneous interfaces offer a promising platform for accelerating alkaline HER, as different components can be assigned complementary catalytic functions. In a typical bifunctional architecture, an oxophilic component promotes water adsorption[12] and dissociation, while a metallic or alloy component provides favorable electronic conductivity and hydrogen-evolution capability. Such spatial decoupling can, in principle, enable hydrogen spillover[13], where H* generated on one domain migrates across the interface and is consumed on an adjacent domain for H_2 formation. Accordingly, metal/oxide, alloy/oxide, carbide/oxide, and phosphide/oxide heterostructures have been widely explored as alkaline HER catalysts[14]. Nevertheless, the physical coexistence of water-activation and hydrogen-evolution domains does not necessarily guarantee efficient spillover[15]. Once H* is

© The Author(s) 2026. Published by Tsinghua University Press. The articles published in this open access journal are distributed under the terms of the Creative Commons Attribution 4.0 International License (http://creativecommons.org/licenses/by/4.0/), which permits use, distribution and reproduction in any medium, provided the original work is properly cited.

Address correspondence to Lin Zeng, zengl3@sustech.edu.cn

Just Accepted

generated, it must cross the interfacial boundary without becoming immobilized by local electronic heterogeneity. In many alloy/oxide heterostructures, a large electronic potential mismatch between the contacted phases can induce pronounced charge redistribution, frontier-state localization, and excessive H* stabilization at the boundary[16]. Under these circumstances, the heterointerface behaves as a hydrogen-trapping region rather than a hydrogen-relay junction, interrupting the continuous delivery and consumption of H* under operating conditions[17].

This issue highlights an important but insufficiently resolved design criterion for spillover-assisted alkaline HER: the interfacial electronic environment must balance transient H* accommodation with facile H* mobility[18]. A relay-competent interface should provide enough stabilization to guide H* across bridge sites, while avoiding strong localization that blocks cross-interface migration. Thus, the central task is not simply to increase the number of active sites or to strengthen hydrogen adsorption, but to engineer electronic continuity across the heterointerface. In this context, converting an interfacial H*-trapping boundary into a relay-permissive junction requires deliberate regulation of local contact-potential mismatch, charge polarization, orbital hybridization, and adsorption thermodynamics at the contacted phases. Establishing such a trap-to-relay conversion is particularly important for high-current alkaline water electrolysis, where H* intermediates must be generated, transferred, and consumed continuously at technologically relevant rates[19].

MoO_2/Ni_4Mo represents a suitable alloy/oxide model system for constructing such an interfacial hydrogen-relay pathway. MoO_2 possesses an oxophilic surface environment that can facilitate water activation, while Ni_4Mo offers high electronic conductivity and favorable hydrogen-evolution characteristics[20]. Their intimate alloy/oxide contact is expected to couple oxide-side water dissociation with alloy-side H_2 formation through interfacial H* migration[11]. However, the intrinsic electronic mismatch between oxide and alloy domains may still cause localized interfacial charge accumulation and H* trapping, limiting the continuity of hydrogen spillover. Introducing an oxide-side electronic regulator offers a possible route to overcome this limitation. Lanthanum is particularly appealing for this purpose because of its strong affinity toward oxygen and its ability to perturb local coordination, defect chemistry[21], and electrostatic fields in oxide environments. Rather than serving as an independent metallic HER site, oxide-coordinated La can be used to reshape the electronic landscape adjacent to the MoO_2/Ni_4Mo boundary, thereby regulating the local H* relay behavior.

Here, we report a La-regulated MoO_2/Ni_4Mo heterostructure for spillover-assisted alkaline hydrogen evolution. The optimized catalyst preserves the dual-phase alloy/oxide architecture, in which Ni_4Mo nanoparticles are generated in situ on MoO_2 rods, while La is preferentially accommodated in the oxide-side environment. Structural, spectroscopic, and theoretical analyses reveal that La relaxes the local potential mismatch, suppresses excessive frontier-state localization, and converts the interfacial bridge site into a more thermoneutral H* relay state. Electrochemical and isotope-sensitive measurements further show accelerated H* adsorption-transfer-desorption kinetics and a reduced isotope-sensitive transfer penalty. As a result, La-MoO_2/Ni_4Mo exhibits outstanding alkaline HER activity with an overpotential of 14 mV at 10 mA cm^{-2} and a Tafel slope of 31.9 mV dec^{-1}. When implemented as the cathode in an AEMWE, it delivers 1 A cm^{-2} at a cell voltage of 1.74 V and sustains stable operation for 1000 h at 70 ℃. This work demonstrates that oxide-side lanthanum-mediated interfacial electronic regulation is an effective strategy for constructing spillover-active, non-precious HER electrodes for practical alkaline water electrolysis.

2 Results and Discussion

2.1 Electrocatalyst synthesis and characterization

To establish a structurally well-defined platform for interfacial electronic regulation, a series of La-regulated MoO_2/Ni_4Mo electrodes with different La precursor contents was first prepared. Preliminary electrochemical screening of *x*%La-MoO_2/Ni_4Mo samples identified 2%La-MoO_2/Ni_4Mo as the optimized sample (Figures S1 and S14). The actual elemental composition of the catalyst was further quantified by inductively coupled plasma optical emission spectroscopy (ICP-OES, Table S1). Unless otherwise stated, La-MoO_2/Ni_4Mo hereafter refers to the optimized 2%La-MoO_2/Ni_4Mo electrode, which is used for mechanistic comparison with pristine MoO_2/Ni_4Mo. This arrangement separates the concentration-dependent optimization from the mechanistic discussion, while ensuring that subsequent structural, spectroscopic, electrochemical, and theoretical analyses focus on the catalytically most relevant interface.

The synthetic strategy is illustrated in Figure 1a. A La-containing $NiMoO_4$ precursor was first grown on Ni foam through a hydrothermal process (Figures S2 and S3), followed by rapid reductive annealing under Ar/H_2 to generate the final La-MoO_2/Ni_4Mo heterostructure. La is expected to be incorporated preferentially into the oxide-side environment rather than acting as a separate metallic active phase. Therefore, Figure 1 focuses on three structural prerequisites for the proposed mechanism: the formation of an authentic MoO_2/Ni_4Mo interface, the preservation of the overall electrode architecture, and the oxide-side localization of La. The morphology of La-MoO_2/Ni_4Mo was first examined by electron microscopy. As shown in Figure 1b, the electrodes maintained a dense array structure of rod-shaped particles with in-situ loaded particles on the Ni foam substrate, and the morphologies of the catalysts with different La contents did not show

Just Accepted

any significant changes (Figure S4). Higher-magnification imaging further reveals that the rod surface is decorated with abundant nanoparticles (Figure 1c), indicating that the metallic Ni_4Mo domains are formed through in situ exsolution during reductive conversion. This architecture is important because it maximizes the number of alloy/oxide contact regions while avoiding severe morphological reconstruction after La introduction. Direct evidence for the alloy/oxide heterointerface is provided by high-resolution transmission electron microscopy (HRTEM). As shown in Figure 1d, lattice fringes with spacings of 0.208 and 0.342 nm can be assigned to the (121) plane of Ni_4Mo and the (011) plane of MoO_2 phases, respectively. The two lattice domains are in direct contact within the same local region, confirming the formation of an authentic MoO_2/Ni_4Mo heterointerface (Figures S5 and S6). Such intimate interfacial contact provides the structural basis for cross-interface H* relay, because the hydrogen intermediate generated on the oxide side can access adjacent metallic Ni_4Mo domains through a short interfacial pathway. The spatial distribution of La was then examined to clarify its role in the heterostructure. Elemental mapping confirms the coexistence of La, Ni, Mo, and O throughout the rod-like structure. Ni is mainly concentrated in the surface nanoparticles, whereas La is enriched in the oxide-rich rod matrix. (Figures 1e, S7 and S8). More importantly, the processed electron energy-loss spectroscopy (EELS) maps derived from the O K-edge and La $M_{4,5}$-edge signals show that the La signal is spatially correlated with the O-rich region and is mainly located within or near the oxide matrix (Figures 1f and 1g). In contrast, no obvious La enrichment is observed in the nanoparticle-rich metallic domains (Figure S9). These results indicate that La is not incorporated as a major alloying element in Ni_4Mo, but instead functions primarily as an oxide-side interfacial regulator. This distinction is essential for the present mechanism, because the role of La is not to create an isolated La-centered hydrogen-evolution site, but to perturb the local Mo-O coordination and electronic environment adjacent to the MoO_2/Ni_4Mo boundary.

The phase constitution and local oxide-side perturbation were further verified by X-ray diffraction (XRD), X-ray photoelectron spectroscopy (XPS), and electron paramagnetic resonance (EPR) analyses. As shown in Figure 1h, the main diffraction features can be indexed to the coexistence of Ni_4Mo (PDF#03-1036) and MoO_2 (PDF#32-0671), demonstrating that the dual-phase alloy/oxide configuration is retained after La incorporation. The enlarged patterns in Figure 1i further show a slight peak shift after La regulation, consistent with subtle lattice expansion and local structural perturbation rather than phase destruction. This observation agrees well with the microscopy results, namely that La incorporation does not alter the fundamental MoO_2/Ni_4Mo heterostructure, but instead perturbs the local environment in a relatively mild way. Raman spectroscopy of the final product (Figure S10) further confirms the structural integrity of the MoO_2 framework. In the low-wavenumber region, the bands at 197, 276, and 345 cm^{-1} can be assigned to phonon modes and Mo-O-Mo bending vibrations of MoO_2, while the peaks at 818.9, 893.1, and 940.1 cm^{-1} correspond to Mo-O stretching modes, collectively indicating that the oxide rod matrix remains structurally preserved after reductive conversion. Further evidence for local oxide-side regulation is obtained from the O 1s and EPR analyses. As shown in Figure 1j, deconvolution of the O 1s spectra reveals a redistribution of oxygen-related species after La incorporation, indicative of a modified local coordination environment on the oxide side. Consistently, Figure 1k shows a strengthened defect-related EPR response, suggesting the variation of oxygen-vacancy-associated species after La regulation. These spectroscopic signatures, together with the preferential oxide-side localization of La revealed by EELS, demonstrate that La primarily rewrites the local environment of the MoO_2 domain rather than reconstructing the overall phase architecture. In this sense, La incorporation selectively tailors the oxide-side coordination and defect chemistry, thereby establishing the structural basis for the subsequent interfacial electronic reconfiguration and the regulation of H* transfer across the heterointerface.

Just Accepted

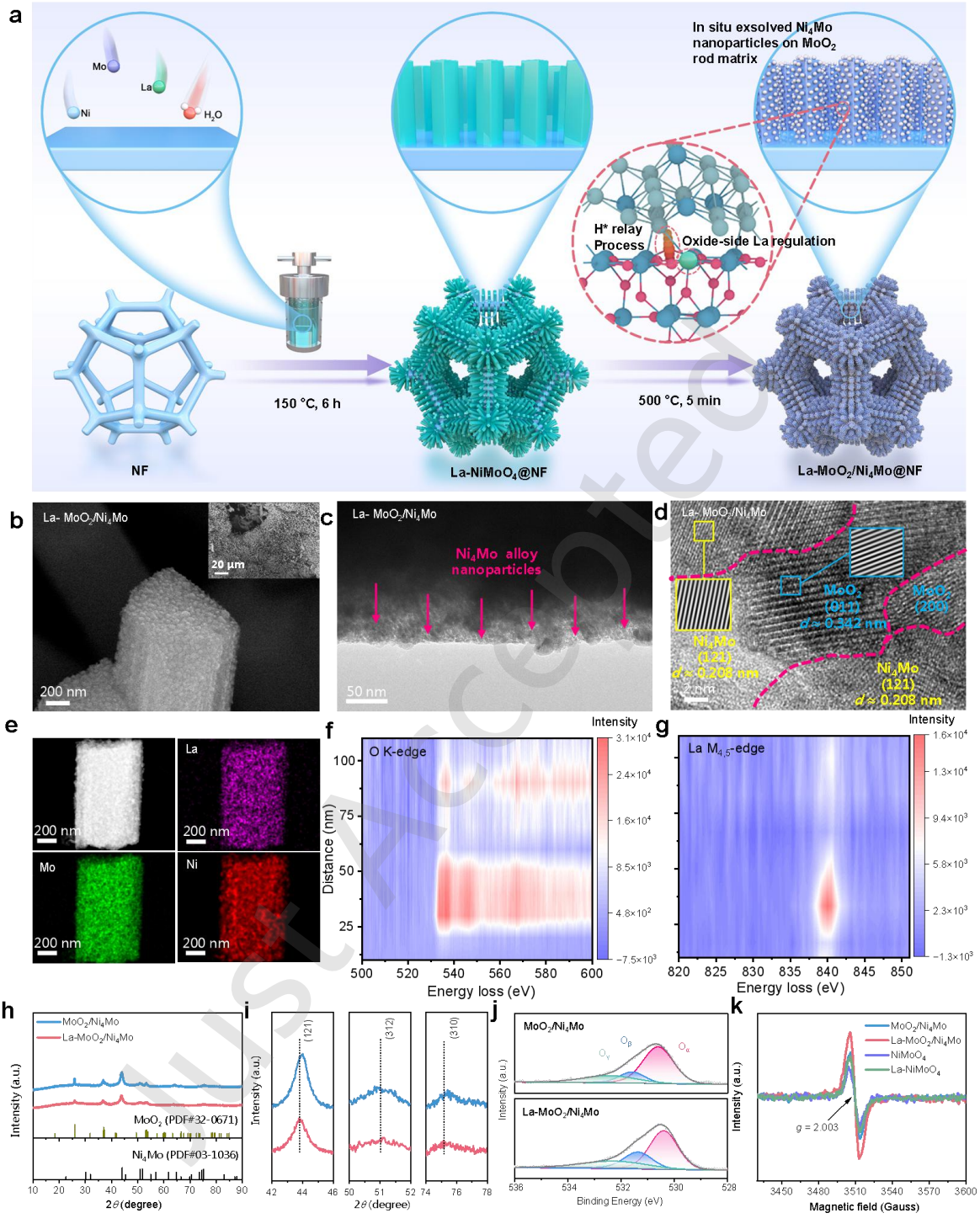


Figure 1. Construction of an oxide-side La-regulated MoO_2/Ni_4Mo heterostructure. (a) Schematic illustration of the precursor-to-heterostructure transformation from La-containing $NiMoO_4$ on Ni foam to La-MoO_2/Ni_4Mo. (b) Scanning electron microscopy (SEM) image of La-MoO_2/Ni_4Mo. (c, d) HRTEM images of the La-MoO_2/Ni_4Mo. (e) Elemental mapping images of La-MoO_2/Ni_4Mo. (f, g) Aberration-corrected electron energy-loss spectroscopy (AC-EELS) maps of O K-edge and La $M_{4,5}$-edge. (h, i) XRD patterns and enlarged views. (j) O 1s XPS. (k) EPR spectra.

Having established the structural basis of the oxide-side La-regulated MoO_2/Ni_4Mo interface, we next examined how La reshapes the interfacial electronic landscape. In spillover-assisted alkaline HER, an alloy/oxide interface must not only provide adjacent water-activation and hydrogen-evolution domains, but also allow H* intermediates to migrate across the boundary without being trapped by localized electronic states. The schematic in Figure 2a illustrates the proposed role of La in reducing local contact-potential mismatch and converting the interfacial region from a H*-trapping boundary into a relay-permissive junction. Atomic force

Just Accepted

microscopy (AFM) and Kelvin probe force microscopy (KPFM) provide direct evidence for this electronic homogenization[19]. The pristine MoO_2/Ni_4Mo heterostructure displays a pronounced contact-potential difference between the particle-rich region and the surrounding oxide rod, whereas La-MoO_2/Ni_4Mo exhibits a markedly reduced spatial potential contrast. The decrease in the contact-potential contrast (ΔCPD) from approximately 80-120 mV to 40-70 mV indicates that La regulation alleviates the local electronic mismatch across the alloy/oxide interface (Figures 2b and 2c), thereby providing a more balanced electronic environment for cross-interface H* transfer[22].

Density-of-states (DOS) analyses further reveal the electronic origin of this La-mediated interfacial reconfiguration. Layer-resolved DOS calculations show that pristine MoO_2/Ni_4Mo possesses pronounced surface/interfacial-state accumulation near the Fermi level, which is consistent with a localized electronic environment that can increase H* trapping at the boundary. After La regulation, this surface-localized frontier-state contribution is markedly attenuated, decreasing from 15.2 states per eV to 6.0 states per eV. The total DOS at the Fermi level decreases from 43.5 to 28.6 states eV^{-1} but remains finite (Figure 2d and Table S2). This reduction primarily reflects a redistribution of states near the Fermi level, particularly the reduced surface/interfacial contributions. This result indicates that La suppresses excessive interfacial-state localization without interrupting electronic accessibility across the MoO_2/Ni_4Mo junction. The orbital-projected DOS further identifies the nature of the redistributed frontier states (Figures 2e and S11). In MoO_2/Ni_4Mo, the states near the Fermi energy (E_f) states are mainly derived from interfacial Ni-d and Mo-d orbitals, together with participation from the Ni-Mo-O interfacial electronic manifold. After La incorporation, the Ni/Mo/O-derived states are redistributed, whereas the La-d contribution remains weak near E_f and does not form a dominant independent frontier peak. These results rule out the formation of a La-centered HER active state. Instead, La acts as an oxide-side orbital-field regulator that perturbs the local Mo-O coordination environment and reshapes the Ni-Mo-O hybridized electronic manifold at the interface. Such frontier-state redistribution weakens the tendency toward interfacial electronic trapping while preserving the continuous electronic pathway required for subsequent H* relay[23].

XPS further reveals La-induced changes in the local electronic environments of Ni and Mo. The Ni^{2+}- and Mo^{4+}-related components shift to higher binding energies after La incorporation (Figures 2f and 2i), reflecting changes in electronic screening and coordination at the heterointerface. X-ray absorption spectroscopy (XAS) provides further insight into the average electronic states and local coordination structure. As shown in Figures 2g and 2j, the Ni and Mo K-edge X-ray absorption near-edge structure (XANES) spectra show altered edge features after La incorporation, indicating that the oxide-side perturbation propagates into the adjacent Ni/Mo electronic structure. Meanwhile, the Fourier-transformed extended X-ray absorption fine structure (FT-EXAFS) spectra in Figures 2h and 2k show that the coordination peaks around ~2.2 Å, assigned to Ni-Mo/Ni and Mo-Mo/Ni contributions[4, 7], shift toward shorter radial distance after La incorporation. The shortened Ni-Mo/Ni and Mo-Mo/Ni interactions indicate strengthened local bonding and tighter interfacial coupling between the two phases. These results collectively demonstrate that La regulation strengthens the electronic and structural coupling across the MoO_2/Ni_4Mo boundary rather than perturbing either phase in isolation. The local coordination state of La was further examined by La-edge XANES, FT-EXAFS, and extended X-ray absorption fine structure (WT-EXAFS). As shown in Figures 2l-n and S12, La-MoO_2/Ni_4Mo exhibits La-O-dominated coordination features (Figure S13 and Table S3). Together with the oxide-side La distribution identified by EELS and the absence of obvious crystalline La-containing impurity phases, these results suggest that La is mainly accommodated in an oxygen-coordinated oxide-side environment rather than incorporated into the Ni_4Mo alloy as a metallic component.

Just Accepted

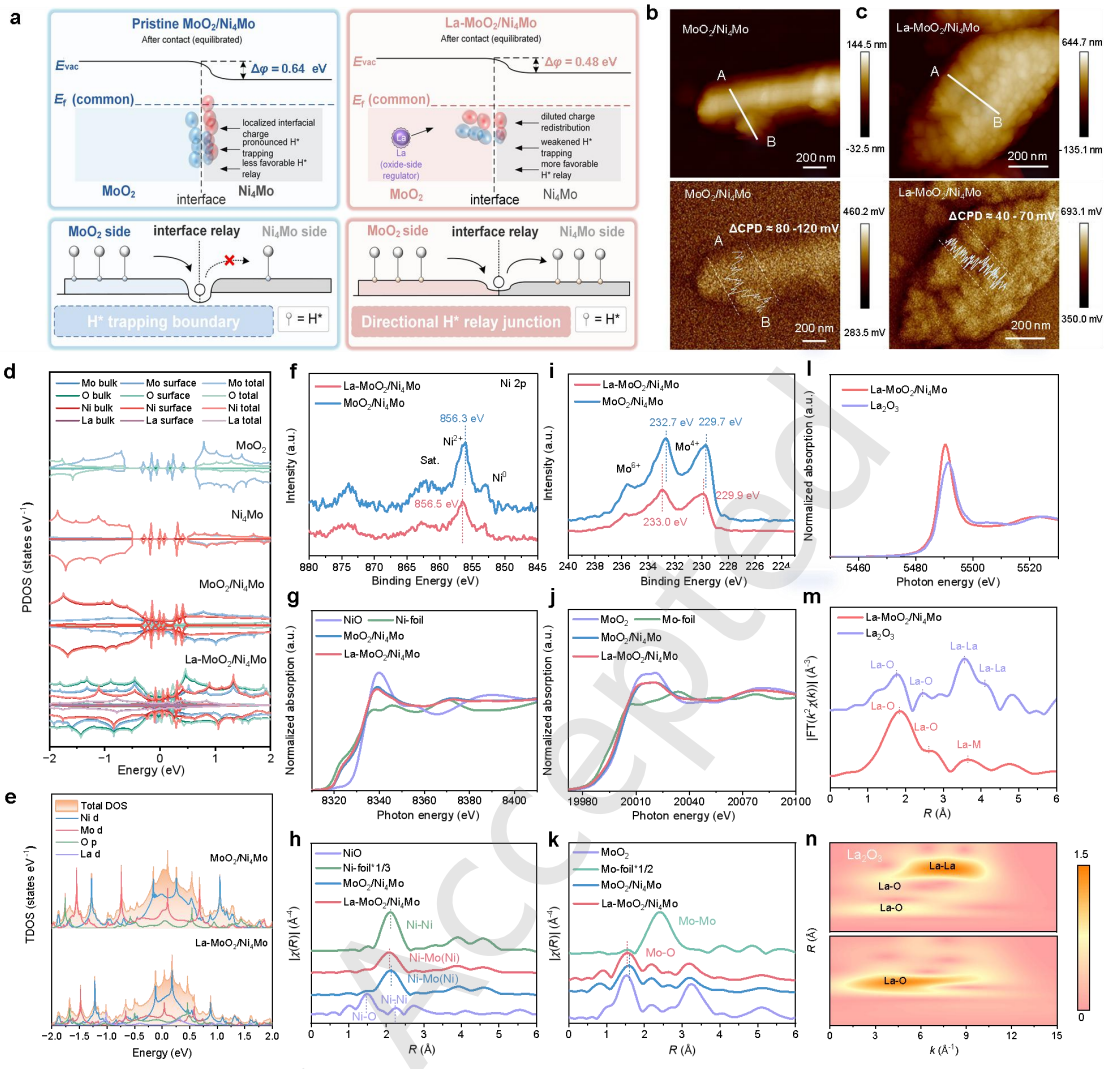


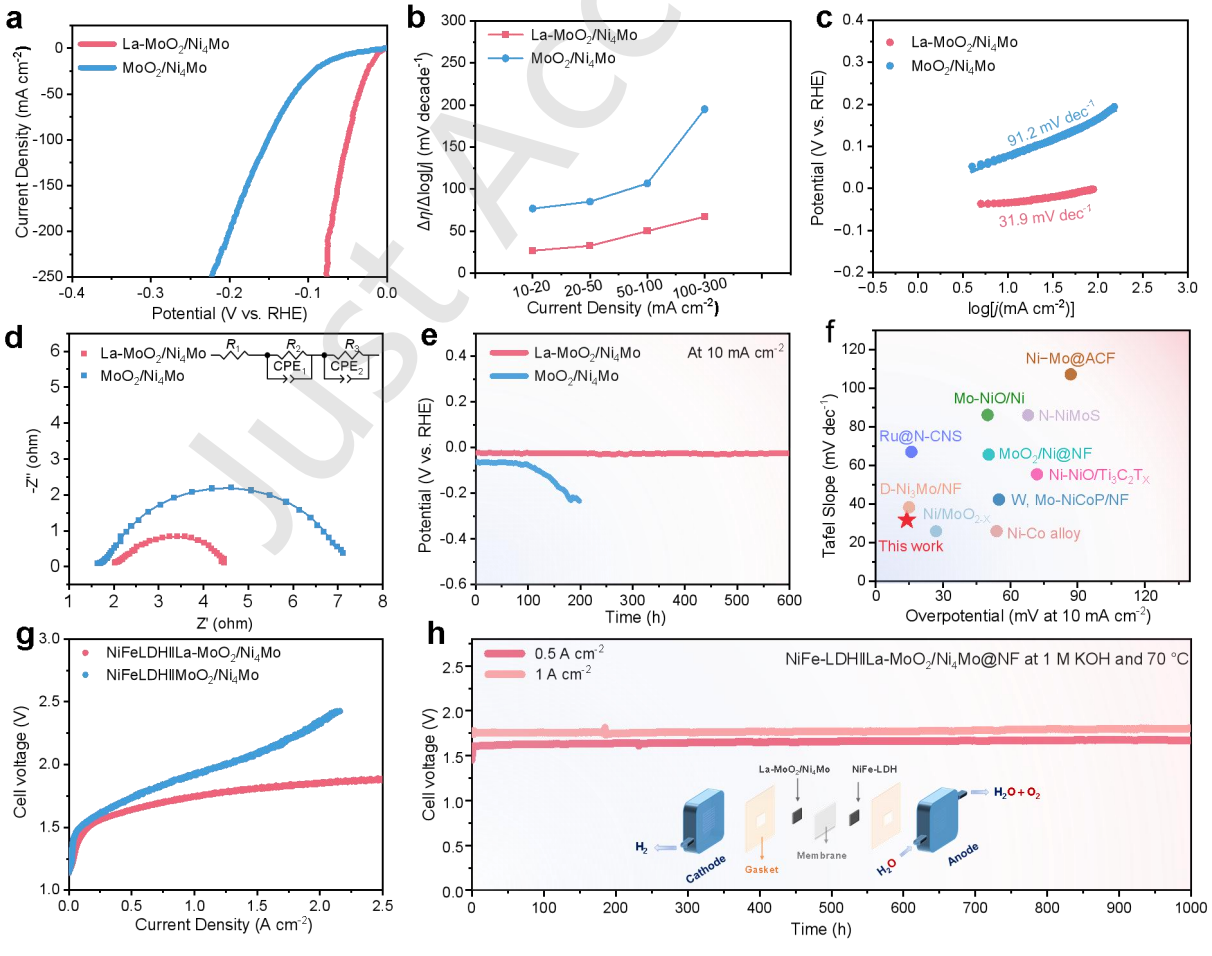
Figure 2. La-mediated electronic trap-to-relay conversion at the MoO_2/Ni_4Mo interface. (a) Schematic illustration of the proposed change in local potential mismatch and interfacial H* transfer barrier before and after La incorporation. (b, c) AFM topography and KPFM potential maps of MoO_2/Ni_4Mo and La-MoO_2/Ni_4Mo. (d) Layer-resolved projected density of states of MoO_2, Ni_4Mo, MoO_2/Ni_4Mo, and La-MoO_2/Ni_4Mo, separating surface/interfacial and bulk-like contributions in the slab models. (e) Element- and orbital-projected DOS of the interfacial layer in MoO_2/Ni_4Mo, and La-MoO_2/Ni_4Mo. (f, i) High-resolution Ni 2p and Mo 3d XPS spectra. (g, j) Ni and Mo K-edge XANES spectra. (h, k) Fourier-transformed EXAFS spectra of Ni and Mo K-edge. (l-n) La-edge XANES / FT-EXAFS / WT-EXAFS.

2.2 Electrocatalytic HER performance

After establishing that La regulation relaxes the electronic mismatch and suppresses excessive frontier-state localization at the MoO_2/Ni_4Mo boundary, we evaluated whether such interfacial electronic reconfiguration translates into improved alkaline HER performance. The electrocatalytic HER performance of the La-regulated MoO_2/Ni_4Mo was evaluated in alkaline electrolyte using a three-electrode configuration. As shown in Figure 3a, La-MoO_2/Ni_4Mo exhibits a markedly enhanced polarization response relative to MoO_2/Ni_4Mo, the La-MoO_2/Ni_4Mo delivers the lowest overpotential of 14 mV at 10 mA cm^{-2}, significantly outperforming MoO_2/Ni_4Mo (59 mV). The improvement extends beyond the low-current region. The conventional Tafel slope is obtained by linear fitting over a selected current-density range, whereas the current-dependent slope ($\Delta\eta/\Delta\log|j|$, where η is the overpotential and j is the current density)[21] captures the local change in overpotential with increasing current density. The latter remains consistently lower for La-MoO_2/Ni_4Mo than for pristine MoO_2/Ni_4Mo (Figure 3b), indicating that La regulation reduces the additional overpotential required as current density increases. This behavior is particularly relevant at elevated current densities, where HER performance is more strongly influenced by interfacial hydrogen transfer, gas evolution, and sustained charge and mass transport. The lower current-dependent slope suggests that La regulation helps maintain a more favorable polarization response as current density increases. Conventional Tafel analysis further confirms the improved HER kinetics: La-MoO_2/Ni_4Mo has a Tafel slope of 31.9 mV dec^{-1}, compared

Just Accepted

with 91.2 mV dec^{-1} for MoO_2/Ni_4Mo (Figure 3c). Commercial Pt/C was tested under identical conditions, giving an overpotential of 29.5 mV at 10 mA cm^{-2} and a Tafel slope of 51.2 mV dec^{-1} (Figure S15). Both values are higher than those for La-MoO_2/Ni_4Mo, indicating better HER performance for the La-regulated heterostructure under these conditions. The double-layer capacitance (C_{dl}) and electrochemical impedance spectroscopy (EIS) results are summarized in Figures 3d and S14, showing that La-MoO_2/Ni_4Mo exhibits the largest C_{dl} and smallest charge-transfer resistance, indicating larger electrochemically active surface area (ECSA) and facilitated interfacial kinetics. Water contact-angle measurements show faster water penetration on La-MoO_2/Ni_4Mo than on pristine MoO_2/Ni_4Mo (Figure S16), indicating improved surface wettability after La incorporation. This improvement may facilitate electrolyte access during HER. The durability of the catalyst was examined under continuous electrolysis in a three-electrode configuration. As shown in Figure 3e, the optimized La-regulated electrode exhibits a much smaller potential drift during prolonged operation than the undoped counterpart, indicating improved structural robustness and catalytic durability. This result suggests that La incorporation stabilizes the operative heterointerface under cathodic polarization, which is consistent with the strengthened local bonding interactions revealed by synchrotron analysis. Furthermore, comparison with representative non-precious HER electrocatalysts reported in the literature under the same electrolyte conditions (1 M KOH; Figure 3f) places the present catalyst among the most competitive systems in terms of the combined metrics of activity. The practical relevance of this catalyst was further evaluated in an AEMWE. As shown in Figures 3g and 3h, the device assembled with the optimized catalyst delivers a cell voltage of 1.74 V at 1 A cm^{-2} and sustains stable operation for 1000 h at 70 ℃, demonstrating its capability under industrially relevant current density. SEM and XRD were used to examine the structural evolution of La-MoO_2/Ni_4Mo after the AEMWE durability test (Figures S17 and S18). These results provide additional evidence regarding the electrode's structural stability during prolonged cathodic operation. The corresponding AEMWE polarization behavior and long-term durability collectively confirm that the activity enhancement achieved in the three-electrode configuration can be effectively translated to device-level water electrolysis. Overall, these electrochemical results establish that appropriate La regulation markedly enhances HER activity, accelerates reaction kinetics across both low and high-current-density regimes, and enables durable AEMWE operation.



Just Accepted

Figure 3. Electrochemical performance of catalysts. (a) Polarization curves. (b) Summary of $\Delta\eta/\Delta\log|j|$ values. (c) Tafel slopes. (d) EIS plot. (e) Chronopotentiometric curves at 10 mA cm^{-2}. (f) Comparison of Tafel slopes and overpotentials at 10 mA cm^{-2} between La-MoO_2/Ni_4Mo and previously reported catalysts[24-33]. (g) AEMWE polarization curves. (h) Long-term AEMWE durability test.

2.3 Electrochemical and isotopic evidence for facilitated interfacial hydrogen relay

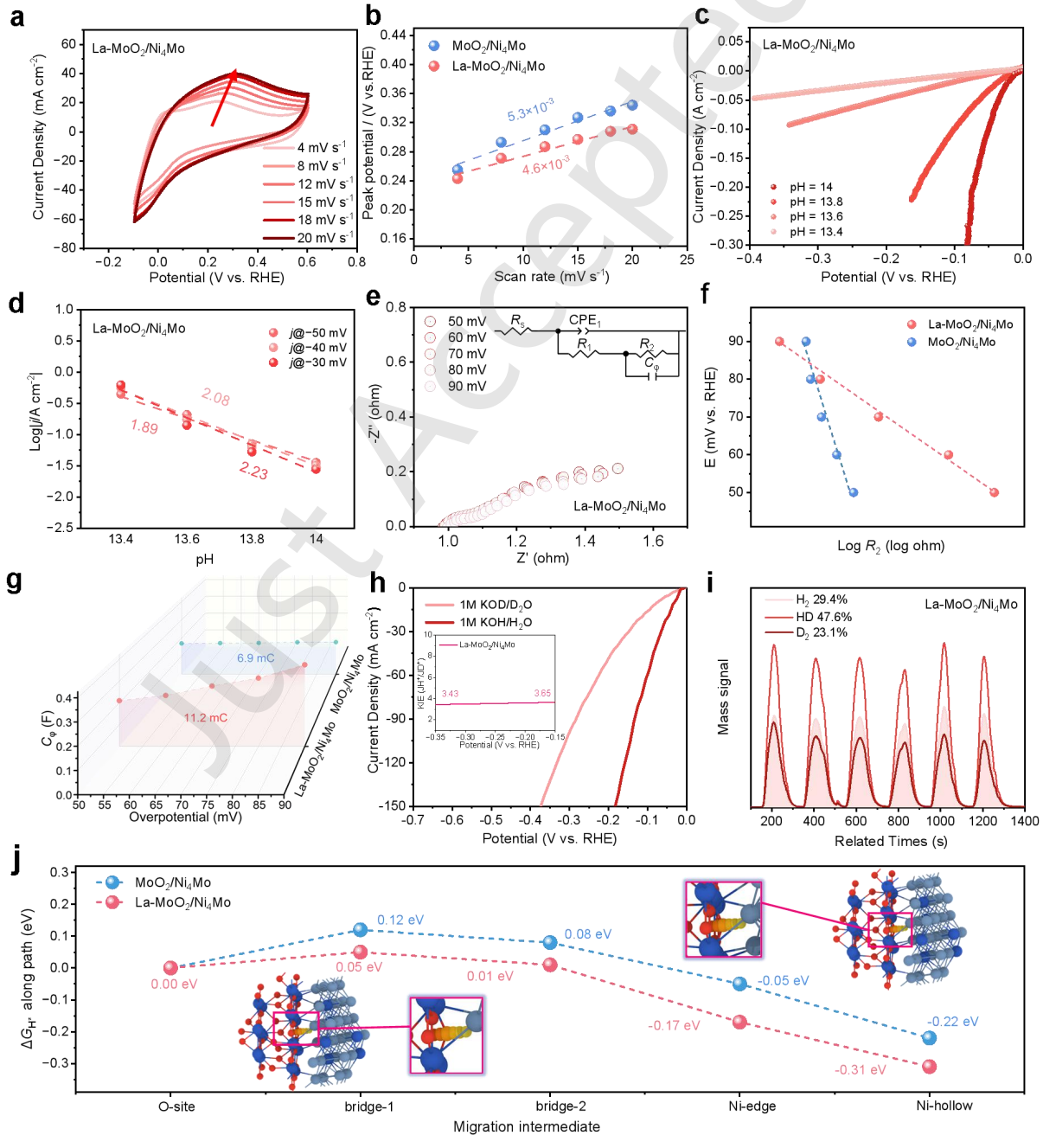
Having established the La-mediated electronic reconfiguration at the MoO_2/Ni_4Mo boundary, we next examined whether this electronic modulation translates into a kinetically more accessible interfacial hydrogen-relay process under operating conditions. In the scan-rate-dependent cyclic voltammetry measurements (Figures 4a and S19), La-MoO_2/Ni_4Mo exhibits a more pronounced hydrogen desorption feature than the undoped MoO_2/Ni_4Mo counterpart. Quantitative analysis of the desorption response (Figure 4b) reveals both a lower scan-rate dependence and a more favorable Tafel-type relationship for La-MoO_2/Ni_4Mo, indicating accelerated hydrogen desorption kinetics after La incorporation[34]. These results suggest that the operative heterointerface in the La-regulated catalyst enables faster turnover of surface hydrogen intermediates, rather than merely strengthening H* retention. The pH-dependent HER response provides additional kinetic information on hydrogen-transfer-related steps. As shown in Figures 4c and S20, the polarization behavior of La-MoO_2/Ni_4Mo displays a stronger dependence on proton/water activity than that of pristine MoO_2/Ni_4Mo. The reaction-order analysis derived from $\log|j|$-pH fitting (Figures 4d and S21) shows that La-MoO_2/Ni_4Mo approaches a more kinetically accessible hydrogen-transfer regime[35], whereas pristine MoO_2/Ni_4Mo is impeded by interfacial transfer resistance. This result indicates that hydrogen evolution on the La-regulated catalyst is less impeded by interfacial H* migration and is more consistent with a kinetically unblocked hydrogen-transfer pathway, pointing to facilitated proton/hydrogen relay at the heterointerface after La incorporation.

To gain further insight into the interfacial H*-transfer process, operando EIS was analyzed using the equivalent circuit shown in Figures 4e and S22. In this model, R_s represents the uncompensated ohmic resistance of the electrolyte/current-collector system. The first parallel branch, consisting of R_1 and CPE_1, accounts for the non-ideal interfacial charge-transfer process and the associated double-layer response at the electrolyte/catalyst interface. The second branch, composed of R_2 and C_φ, describes an additional relaxation process associated with hydrogen adsorption. R_2 is an effective kinetic resistance associated with the hydrogen-related interfacial process, whereas C_φ represents the pseudocapacitive response arising from potential-dependent hydrogen adsorption[36]. The fitted parameters are listed in Tables S4 and S5. Accordingly, the hydrogen adsorption charge, Q_H, can be obtained by integrating the C_φ-potential profile, whereas the potential dependence of R_2 provides a kinetic descriptor for the hydrogen-related interfacial process. This assignment is consistent with previous spillover studies, in which R_2 and C_φ were used to describe the resistance and pseudocapacitance of active hydrogen adsorption at heterointerfaces[37]. However, individual circuit elements cannot uniquely identify a single elementary reaction step. The R_2-C_φ branch is therefore interpreted as a hydrogen-related kinetic contribution; its association with interfacial hydrogen transfer is supported by the complementary electrochemical and theoretical results. As shown in Figure 4f, the Tafel slope derived from the relationship between $\log|R_2|$ and potential is markedly smaller for La-MoO_2/Ni_4Mo than for MoO_2/Ni_4Mo, indicating a reduced potential-dependent kinetic penalty for the hydrogen-related interfacial process after La regulation. This behavior is consistent with accelerated spillover-assisted hydrogen relay across the alloy/oxide junction. Additional evidence is obtained from the interfacial pseudocapacitive response. The C_φ-potential profiles and their integrated charge (Figure 4g) show that La-MoO_2/Ni_4Mo possesses a substantially larger hydrogen-related charge (Q_H) than the undoped heterostructure (11.2 vs. 6.9 mC). The larger Q_H indicates that the La-regulated catalyst can accumulate and utilize a greater population of electrochemically accessible hydrogen intermediates under working conditions. Importantly, when considered together with the more favorable desorption kinetics and the smaller R_2-derived Tafel slope, this increase in Q_H shows a more efficient and dynamically sustainable H* adsorption-transfer-desorption sequence. The Bode phase-angle plots in Figure S23 provide supplementary information on the interfacial response under HER bias[34, 38]. In general, the low-frequency region is associated with the charge-transfer process at the electrolyte/catalyst interface, whereas the high-frequency response is more closely related to inner-layer or interfacial conduction. Compared with the undoped sample, La-MoO_2/Ni_4Mo shows a slightly more pronounced phase-angle evolution with increasing overpotential. Although the difference is not dramatic, this trend is consistent with a somewhat more responsive heterointerface under operating conditions, in line with the accelerated H-transfer kinetics inferred from the fitted EIS parameters.

To further verify whether the kinetic enhancement identified above is indeed associated with interfacial hydrogen transfer, isotope-sensitive experiments were performed by combining kinetic isotope effect (KIE) analysis with operando differential electrochemical mass spectrometry (DEMS) (Figure S24). In hydrogen-spillover systems, KIE values larger than unity indicate that hydrogen-transfer-related steps are kinetically involved, whereas lower and less potential-dependent KIE values imply a reduced kinetic penalty for this isotope-sensitive process. Under D_2O/KOD conditions, for the undoped MoO_2/Ni_4Mo, the KIE increases from 3.80 to 5.74 (Figure

Just Accepted

S25), indicating a strong and increasingly potential-dependent isotope penalty. In contrast, La-MoO_2/Ni_4Mo exhibits lower and much flatter KIE values in the range of 3.43 to 3.65 (Figure 4h). Since both catalysts still show KIE values well above unity, hydrogen transfer remains kinetically involved in both cases[23, 39-40]. However, the smaller and stable KIE of La-MoO_2/Ni_4Mo indicates that the hydrogen-transfer step becomes less hindered after La regulation. In other words, La does not bypass the hydrogen-transfer pathway, but lowers its kinetic penalty, which is fully consistent with the accelerated H* relay inferred from the electrochemical analyses. Operando DEMS in a mixed-isotope electrolyte was further used to probe isotope-output behavior. In 1 M KOD with H_2O:D_2O = 1:4, the electrolyte is D-rich, and the D_2-related signal is sensitive to whether D* intermediates can effectively participate in interfacial transfer and recombination. As shown in Figure 4i, La-MoO_2/Ni_4Mo displays a higher normalized D_2 ion-current contribution (23.1%) than pristine MoO_2/Ni_4Mo (13.8%, Figure S26), together with a more sustained isotope-output response. Since D* transfer is intrinsically more sluggish than H* transfer, the enhanced D_2-related contribution suggests that La regulation makes D*-involved relay less kinetically blocked. The DEMS result therefore provides isotope-resolved kinetic evidence for a more accessible H/D relay process. The background-corrected integrated DEMS ion-current signals and the corresponding normalized isotope-output distributions of H_2, HD, and D_2 are summarized in Tables S6 and S7.



Just Accepted

Figure 4. Electrochemical, isotope-sensitive, and computational validation of interfacial H*-transfer. (a) Scan-rate-dependent cyclic voltammetry. (b) Kinetic analysis of the hydrogen desorption feature. (c, d) pH-dependent HER kinetics and the corresponding reaction-order analysis. (e) Representative operando EIS spectra and equivalent circuit containing the H*-adsorption/transfer-related (R_2-C_φ) branch. (f) Tafel plots derived from the relationship between log|R_2| and potential. (g) C_φ-derived hydrogen-related charge analysis. (h) Isotope polarization curves in H_2O/KOH and D_2O/KOD with the inset showing the corresponding KIE values. (i) Operando DEMS isotope-output profiles and normalized ion-current contributions of H_2, HD, and D_2 over La-MoO_2/Ni_4Mo in mixed H_2O/D_2O electrolyte. (j) Computed interfacial H* migration pathway from the MoO_2 side to the Ni_4Mo side.

2.4 Theoretical Insights of La-Enabled Trap-to-Relay Conversion

To establish a microscopic mechanistic picture for the La-enabled interfacial hydrogen relay, Density Functional Theory (DFT) calculations were performed on MoO_2, Ni_4Mo, MoO_2/Ni_4Mo, and La-MoO_2/Ni_4Mo models. Instead of relying on a single H* adsorption descriptor, the calculations correlate interfacial potential mismatch, charge redistribution, H* thermodynamics, cross-interface migration barriers, and elementary HER free-energy profiles. The work-function analysis first reveals the intrinsic electronic mismatch between the oxide and alloy components. MoO_2 and Ni_4Mo exhibit work functions of 5.72 and 4.61 eV, respectively, indicating a substantial electronic potential difference across the oxide/alloy boundary (Figure 5a). After the formation of the MoO_2/Ni_4Mo interface, the effective work function is 5.08 eV, while La incorporation decreases it to 4.92 eV. More importantly, the effective interfacial mismatch ($\Delta\varphi$) decreases from 0.64 to 0.48 eV after La regulation. The planar-averaged electrostatic-potential profiles further show that La-MoO_2/Ni_4Mo exhibits a smoother potential transition with reduced oscillation amplitude across the interface (Figures 5b and S27). Consistent with the reduced local potential contrast measured by KPFM (Figures 2b and 2c), the smaller interfacial work-function mismatch and smoother electrostatic-potential profile indicate that oxide-side La regulation reduces interfacial charge polarization and creates a more uniform electronic environment for H* transfer across the MoO_2/Ni_4Mo junction[41].

Differential charge-density maps provide a spatial view of this interfacial electronic reconfiguration. In pristine MoO_2/Ni_4Mo, charge accumulation and depletion are more strongly localized near the narrow contact region, consistent with a more pronounced interfacial dipole and a stronger local trapping tendency (Figure 5c)[39]. After La regulation, the charge redistribution becomes more spatially dispersed, suggesting a weakened localized electronic trap at the boundary. This behavior is consistent with the oxide-side regulatory role of La, which perturbs the nearby coordination environment and modulates the charge polarization at the MoO_2/Ni_4Mo contact without acting as a new metallic hydrogen-evolution center. The calculated H* adsorption free energies (ΔG_H*) further clarify how this electronic redistribution affects the interfacial relay sites (Figure 5d). For pristine MoO_2/Ni_4Mo, the ΔG_H* at the MoO_2-side, bridge, and Ni_4Mo-side sites are -0.37, -0.11, and -0.55 eV, respectively. The bridge site is already relatively close to thermoneutrality, but still retains a weak trapping character. After La regulation, the corresponding values shift to -0.29, -0.02, and -0.48 eV. In particular, the ΔG_H* of bridge-site approaches 0 eV, indicating that La does not introduce a new La-centered H-binding site, but converts the interfacial bridge into a more suitable relay state that can temporarily accommodate H without forming a deep trap. Meanwhile, the Ni_4Mo side remains the thermodynamically preferred final state, favoring subsequent H_2 release after cross-interface transfer.

The complete free-energy landscape confirms that La regulation optimizes the entire spillover-assisted HER pathway, with the most prominent effect occurring at the interfacial H* transfer step (Figure 5e). The dominant pathway corresponds to H* migration from the MoO_2 side to the Ni_4Mo side through interfacial bridge states. In pristine MoO_2/Ni_4Mo, this pathway exhibits a barrier of 0.41 eV, whereas La-MoO_2/Ni_4Mo lowers the barrier to 0.22 eV and stabilizes the final Ni_4Mo-side state (Figures 5f and S28). The reverse pathway remains associated with a higher barrier, decreasing only from 0.62 to 0.54 eV (Figure 5g), indicating that La lowers the overall migration resistance while preserving the preferred MoO_2-to-Ni_4Mo relay direction. The flanking elementary steps also benefit from La regulation: the water-dissociation barrier decreases from 0.68 to 0.51 eV, and the H_2-release barrier decreases from 0.44 to 0.33 eV (Figure S29). Nevertheless, the most substantial change is the flattening of the interfacial H* transfer landscape, showing that cross-interface relay is the step most directly optimized by La.

The relationship between interfacial electronic mismatch and H* transfer kinetics is further summarized in Figures 5h and S30. As $\Delta\varphi$ decreases, the H* transfer barrier decreases accordingly, linking the relaxation of the electronic potential mismatch with the lowering of the cross-interface migration penalty. This descriptor correlation supports the mechanistic picture that La acts as an oxide-side interfacial regulator rather than an isolated active center. It weakens localized electronic trapping, shifts the bridge site toward a quasi-thermoneutral relay state, and facilitates directional H* migration from MoO_2 to Ni_4Mo. The free-energy landscapes provide a complementary visualization of the H* relay process (Figure S31). Compared with pristine MoO_2/Ni_4Mo, La-MoO_2/Ni_4Mo exhibits a smoother and less localized energy landscape along the interfacial migration coordinate, consistent with reduced trapping at the contact region and a more continuous bridge-mediated relay channel. These computational results converge with the electronic, electrochemical, and

Just Accepted

isotope-sensitive evidence discussed above, demonstrating that La enables a trap-to-relay conversion at the MoO_2/Ni_4Mo interface. Overall, MoO_2 serves as the oxide-side H* generation region, the bridge site functions as a transient relay state, Ni_4Mo provides the favorable terminal H* stabilization and H_2-release environment, and La electronically couples these functional regions into a continuous spillover pathway.

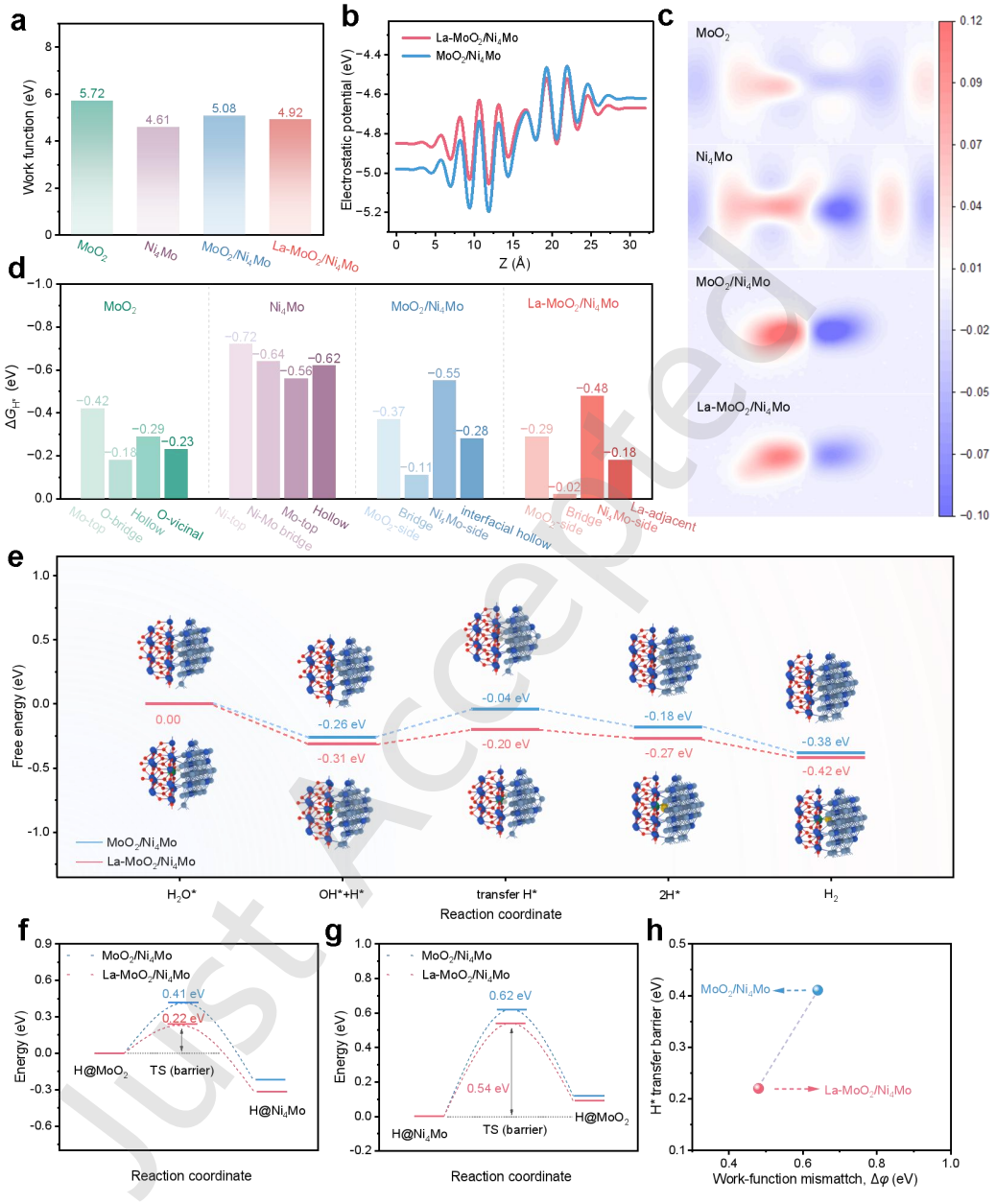


Figure 5 DFT verification of La-enabled trap-to-relay conversion at the MoO_2/Ni_4Mo interface. (a) Work-function summary of MoO_2, Ni_4Mo, MoO_2/Ni_4Mo, and La-MoO_2/Ni_4Mo models. (b) Planar-averaged electrostatic-potential profiles of MoO_2/Ni_4Mo and La-MoO_2/Ni_4Mo. (c) Differential charge-density maps. (d) ΔG_{H^*} values at representative adsorption sites. (e) Overall HER free-energy diagram. (f) Interfacial H* transfer barriers from MoO_2 to Ni_4Mo. (g) Interfacial H* transfer barriers from Ni_4Mo to MoO_2. (h) Correlation between effective interfacial work-function mismatch and H* transfer barrier.

Just Accepted

3 Conclusion

In summary, an oxide-side lanthanum-regulated MoO_2/Ni_4Mo heterostructure was developed as an efficient hydrogen-evolution cathode for alkaline water electrolysis. The in situ formed MoO_2/Ni_4Mo alloy/oxide interface provides a structurally integrated platform for coupling oxide-side water activation with alloy-side hydrogen evolution, while lanthanum is preferentially accommodated within the oxygen-coordinated MoO_2-side environment rather than acting as an independent metallic active center. This spatially selective regulation attenuates the local electronic mismatch across the heterointerface, suppresses excessive near-Fermi-state localization, and converts the interfacial H* bridge from a trapping site into a relay-permissive junction. As a result, the optimized La-MoO_2/Ni_4Mo catalyst exhibits markedly enhanced alkaline HER activity and kinetics, requiring only 14 mV to reach 10 mA cm^{-2} with a Tafel slope of 31.9 mV dec^{-1}. More importantly, the catalyst delivers device-relevant performance in an anion-exchange-membrane water electrolyzer, achieving 1 A cm^{-2} at 1.74 V and stable operation for 1000 h at 70 ℃. Mechanistic studies combining electrochemical kinetics, isotope-sensitive experiments, operando impedance analysis, and theoretical calculations demonstrate that lanthanum regulation lowers the interfacial H* migration barrier and enables a more continuous MoO_2-to-Ni_4Mo hydrogen-relay pathway. These findings highlight interfacial electronic continuity, rather than isolated adsorption optimization alone, as a key design criterion for spillover-assisted alkaline HER catalysts and provide a promising route toward durable non-precious cathodes for practical alkaline water electrolysis.

Acknowledgements

This work was financially supported by the National Natural Science Foundation of China (No. 52276198, 52536003), Shenzhen Science and Technology Plan Project (No. JCYJ20241202125404007, ZDCY20250901100303004), Shenzhen Key Laboratory of Hydrogen Energy (No. ZDSYS20160331101348 98), and High-level of Special Funds (No. G03034K001).

Declaration of conflicting interests

The authors declare no conflicting interests regarding the content of this article.

Data availability

All data needed to support the conclusions in the paper are presented in the manuscript and/or the Supplementary Materials. Additional data related to this paper may be requested from the corresponding author upon request.

Electronic Supplementary Material: Supplementary material (Experimental details, supplementary figures S1-S31 and tables S1-S9) is available in the online version of this article at https://doi.org/10.26599/NRE.2026.9120292.

References

[1] Y. Wang, Y. Zhang, P. Xing, X. Li, Q. Du, X. Fan, Z. Cai, R. Yin, Y. Yao, W. Gan. Self-Encapsulation of High-Entropy Alloy Nanoparticles inside Carbonized Wood for Highly Durable Electrocatalysis. *Advanced Materials* **2024**, *36*, 2402391.

[2] J. Gu, L. Li, Q. Yang, F. Tian, W. Zhao, Y. Xie, J. Yu, A. Zhang, L. Zhang, H. Li, *et al.* Twinning Engineering of Platinum/Iridium Nanonets as Turing-Type Catalysts for Efficient Water Splitting. *Journal of the American Chemical Society* **2024**, *146*, 5355-5365.

[3] Y. Wang, H. Arandiyan, S. S. Mofarah, X. Shen, S. A. Bartlett, P. Koshy, C. C. Sorrell, H. Sun, C. Pozo-Gonzalo, K. Dastafkan, *et al.* Stacking Fault-Enriched $MoNi_4/MoO_2$ Enables High-Performance Hydrogen Evolution. *Advanced Materials* **2024**, *36*, 2402156.

[4] Y. Chang, L. Kong, D. Xu, X. Lu, S. Wang, Y. Li, J. Bao, Y. Wang, Y. Liu. Mo Migration-Induced Crystalline to Amorphous Conversion and Formation of $RuMo/NiMoO_4$ Heterogeneous Nanoarray for Hydrazine-Assisted Water Splitting at Large Current Density. *Angewandte Chemie International Edition* **2024**, *64*, e202414234.

[5] M. Wang, H. Yang, J. Shi, Y. Chen, Y. Zhou, L. Wang, S. Di, X. Zhao, J. Zhong, T. Cheng, *et al.* Alloying Nickel with Molybdenum Significantly Accelerates Alkaline Hydrogen Electrocatalysis. *Angewandte Chemie International Edition* **2021**, *60*, 5771-5777.

[6] A. Bashkatov, F. Bürkle, Ç. Demirkır, W. Ding, V. Sanjay, A. Babich, X. Yang, G. Mutschke, J. Czarske, D. Lohse, *et al.* Electrolyte Droplet Spraying in H_2 Bubbles during Water Electrolysis under Normal and Microgravity Conditions. *Nature Communications* **2025**, *16*, 4580.

[7] J. Song, Y. Q. Jin, L. Zhang, P. Dong, J. Li, F. Xie, H. Zhang, J. Chen, Y. Jin, H. Meng, *et al.* Phase-Separated Mo-Ni Alloy for Hydrogen Oxidation and Evolution Reactions with High Activity and Enhanced Stability. *Advanced Energy Materials* **2021**, *11*, 2003511

[8] Y. Xu, J. Du, J. Jiang, Y. Miao, Z. Zhuang, Z. Liu, Y. Yan, R. Pan, J. Yang, M. Wang, *et al.* Co Nanoparticle: An Efficient H-pump for Pt Single Atoms Towards Enhanced Hydrogen Spillover. *Angewandte Chemie International Edition* **2025**, *64*, e202502227.

[9] K. Yan, B. Wu, Y. Mu, J. Luo, Z. Tang, Q. Zhang, Y. Jiang, X. Zhong, W. Limphirat, Y. Yang, *et al*. Multiscale Engineering of Ni_4Mo/MoO_2 Heterointerfaces on N-doped Vertical Graphene for Efficient AEMWE Hydrogen Evolution. *Applied Catalysis B: Environment and Energy* **2026**, *387*, *126457*.

[10] Z. Chen, G. Liu, Y. Zhao, Y. Yan, Q. Ke, C. Wan, Z. Zhang, J. Yuan, H. Li, M. Liu, *et al*. Co_1Zn Single-Atom Alloy Boosts Active Hydrogen Spillover for Highly Efficient Electrosynthesis of Ammonia over 2 A cm^{-2} Current Density. *Angewandte Chemie International Edition* **2025**, *65*, e23740.

[11] J. Chen, Z. Li, Z. Li, M. Wang, S. Li, Y. Zhou, Y. Lai. Nickel Nano-Network Facilitates Short-Path Hydrogen Spillover for Efficient Alkaline Hydrogen Evolution with High-Current-Densities. *Chemical Communications* **2025**, *61*, 8399-8402.

[12] J. Luo, B. Wu, K. Yan, Y. Mu, Q. Zhang, H. Zou, Z. Tang, G. Zhang, W. Limphirat, W. Li, *et al*. Molten-Salt Flash Synthesis of P-doped Iron Oxide with Engineered Oxygen Vacancies for Lattice-Oxygen Water Oxidation. *Chemical Science* **2026**, *17*, 13550-13561.

[13] H. Shen, F.-Y. Gao, H. Li, J. Xu, M. Jaroniec, Y. Zheng, S.-Z. Qiao. Durable Anion Exchange Membrane Water Electrolysis in Low-Alkaline Concentration Electrolyte. *Journal of the American Chemical Society* **2025**, *147*, 22677-22685.

[14] J. Dai, Y. Zhu, Y. Chen, X. Wen, M. Long, X. Wu, Z. Hu, D. Guan, X. Wang, C. Zhou, *et al*. Hydrogen Spillover in Complex Oxide Multifunctional Sites Improves Acidic Hydrogen Evolution Electrocatalysis. *Nature Communications* **2022**, *13*, 1189.

Just Accepted

[15] W. Guo, G. Zhao, Z. Sun, B. Zhang, D. Xin, M. Gao, Y. Liu, Z. Zhuang, H.-W. Liang, H. Pan, *et al*. Decoupling Fast Hydrogen Oxidation Reaction on a Tandem Electrocatalyst. *Nature Communications* **2025**, *16*, 6741.

[16] C. Han, C. Cheng, W. Lv, L. Xiao, J. Zhang, Y. Zhao, Z. a. Ma, Z. Liu, J. Wang, Q. Yun, *et al*. Hydrogen Spillover Enabled by Edge Dislocations for Efficient Hydrogen Evolution. *Advanced Functional Materials* **2025**, *35*, 2425615

[17] H. Hao, Y. Zhang, Z. Wang, S. Shen, L. Xu, Z. Lv, Y. Shen, B. Wei. Hydrogen Spillover in Superwetting Ni/NiMoN Mott-Schottky Heterostructures for Boosting Ampere-Level Hydrogen Evolution. *Applied Physics Letters* **2025**, *126*, 113901

[18] Y. Yan, J. Du, C. Li, J. Yang, Y. Xu, M. Wang, Y. Li, T. Wang, X. Li, X. Zhang, *et al*. H-Buffer Effects Boosting H-Spillover for Efficient Hydrogen Evolution Reaction. *Energy & Environmental Science* **2024**, *17*, 6024-6033.

[19] J. Li, J. Hu, M. Zhang, W. Gou, S. Zhang, Z. Chen, Y. Qu, Y. Ma. A Fundamental Viewpoint on the Hydrogen Spillover Phenomenon of Electrocatalytic Hydrogen Evolution. *Nature Communications* **2021**, *12*, 3502.

[20] D. Song, J. Roh, J. Choi, H. Lee, G. Koh, Y. Kwon, H. Kim, H. M. Lee, M. Kim, E. Cho. Heterogeneous Structure of Ni-Mo Nanoalloys Decorated on MoO_x for an Efficient Hydrogen Evolution Reaction Using Hydrogen Spillover. *Advanced Science* **2024**, *11*, 2403752.

[21] S. Liu, Z. Zhang, K. Dastafkan, Y. Shen, C. Zhao, M. Wang. Yttrium-Doped NiMo-MoO_2 Heterostructure Electrocatalysts for Hydrogen Production from Alkaline Seawater. *Nature Communications* **2025**, *16*, 773.

[22] J. Li, Y. Ma, J. C. Ho, Y. Qu. Hydrogen Spillover Phenomenon at the Interface of Metal-Supported Electrocatalysts for Hydrogen Evolution. *Accounts of Chemical Research* **2024**, *57*, 895-904.

[23] L. Ren, K. Zhang, Y.-C. Huang, Y. R. Lu, H. Deng, Y. Ding, C. Chen, B. Huang, W. Hua, L. Fu, *et al*. Tailored Interatomic Interactions in High-Entropy Alloys for Enhanced Electrocatalytic Hydrogen Evolution Reaction in Alkaline Water. *ACS Catalysis* **2025**, *15*, 11022-11033.

[24] J. Wu, Y. Zhu, S. Ye, B. He, S. Zhang, H. Pang, C. Jin, L. Chen, D. Sun, L. Xu, *et al*. Synergistic Strong and Reactive Metal-Support Interactions-Induced Electronic Regulation of Sub-2 nm Ru Nanoclusters for Enhanced Hydrogen Evolution Performance. *Chemistry-A European Journal* **2025**, *31*, e202500651.

[25] C. Huang, L. Yu, W. Zhang, Q. Xiao, J. Zhou, Y. Zhang, P. An, J. Zhang, Y. Yu. N-Doped Ni-Mo Based Sulfides for High-Efficiency and Stable Hydrogen Evolution Reaction. *Applied Catalysis B: Environmental* **2020**, *276*, 119137.

[26] X. Guo, M. Li, L. He, S. Geng, F. Tian, Y. Song, W. Yang, Y. Yu. Industrially Promising NiCoP Nanorod Arrays Tailored with Trace W and Mo Atoms for Boosting Large-Current-Density Overall Water Splitting. *Nanoscale* **2021**, *13*, 14179-14185.

[27] J. Shen, Q. Li, W. Zhang, Z. Cai, L. Cui, X. Liu, J. Liu. Spherical Co_3S_4 Grown Directly on Ni-Fe Sulfides as a Porous Nanoplate Array on $FeNi_3$ Foam: A Highly Efficient and Durable Bifunctional Catalyst for Overall Water Splitting. *Journal of Materials Chemistry A* **2022**, *10*, 5442-5451.

[28] B. Zhang, Z. Du, R. Sun, X. Lai, J. Lan, X. Liu, L. Yan. Tremella-Like Ni-NiO with O-Vacancy Heterostructure Nanosheets Grown In Situ on MXenes for Highly Efficient Hydrogen and Oxygen Evolution. *ACS Applied Materials & Interfaces* **2022**, *14*, 47529-47541.

[29] J. Wang, H. Shao, S. Ren, A. Hu, M. Li. Fabrication of Porous Ni-Co Catalytic Electrode with High Performance in Hydrogen Evolution Reaction. *Applied Surface Science* **2021**, *539*, 148045.

[30] W. Liang, P. Dong, Z. Le, X. Lin, X. Gong, F. Xie, H. Zhang, J. Chen, N. Wang, Y. Jin, *et al*. Electron Density Modulation of MoO_2/Ni to Produce Superior Hydrogen Evolution and Oxidation Activities. *ACS Applied Materials & Interfaces* **2021**, *13*, 39470-39479.

[31] J. Huang, J. Han, T. Wu, K. Feng, T. Yao, X. Wang, S. Liu, J. Zhong, Z. Zhang, Y. Zhang, *et al*. Boosting Hydrogen Transfer during Volmer Reaction at Oxides/Metal Nanocomposites for Efficient Alkaline Hydrogen Evolution. *ACS Energy Letters* **2019**, *4*, 3002-3010.

[32] P. Zhou, L. Tao, S. Tao, Y. Li, D. Wang, X. Dong, T. Frauenheim, X. Fu, X. Lv, S. Wang. Construction of Nickel-Based Dual Heterointerfaces towards Accelerated Alkaline Hydrogen Evolution via Boosting Multi-Step Elementary Reaction. *Advanced Functional Materials* **2021**, *31*, 2104827.

[33] W. Liang, M. Zhou, X. Li, L. Zhu, Z. Li, Y. Zhou, J. Chen, F. Xie, H.-F. Wang, N. Wang, *et al*. Oxygen-Vacancy-Rich MoO_2 Supported Nickel as Electrocatalysts to Promote Alkaline Hydrogen Evolution and Oxidation Reactions. *Chemical Engineering Journal* **2023**, *464*, 142671.

[34] S. Pan, C. Li, T. Xiong, Y. Xie, F. Luo, Z. Yang. Hydrogen Spillover in MoO_xRh Hierarchical Nanosheets Boosts Alkaline HER Catalytic Activity. *Applied Catalysis B: Environmental* **2024**, *341*, 123275.

[35] J. Jiang, G. Xu, B. Gong, J. Zhu, W. Wang, T. Zhao, Y. Feng, Q. Wu, S. Liu, L. Zhang. Hydrogen Spillover Mechanism of Superaerophobic $NiSe_2$-Ni_5P_4 Electrocatalyst to Promote Hydrogen Evolution in Saline Water. *Advanced Functional Materials* **2024**, *35*, 2412685

[36] H. L. Su, W. Liao, S. X. Mo, H. Wang, Y. Cao, H. Yu, H. F. Wang. Decoupling Volmer and Tafel Steps via Dual-Site Interface Engineering in Ni/$MoBT_x$ for Efficient Hydrogen Electrocatalysis. *Advanced Functional Materials* **2025**, *36*, e18373.

[37] Y. Li, L. Li, S. Xu, K. Cui, T. Wang, Z. Jiang, J. Li. Hydrogen Spillover Mechanism at the Metal-Metal Interface in Electrocatalytic Hydrogenation. *Angewandte Chemie International Edition* **2024**, *63*, e202407810

[38] C. Xie, W. Chen, S. Du, D. Yan, Y. Zhang, J. Chen, B. Liu, S. Wang. In-Situ Phase Transition of WO_3 Boosting Electron and Hydrogen Transfer for Enhancing Hydrogen Evolution on Pt. *Nano Energy* **2020**, *71*, 104653.

[39] Z. Zhao, Y. Chen, Y. Liu, S. Qin, Z. Li, Z. Zhang, X. Meng. Unveiling In Situ Reconstruction for Dynamically Enhanced Hydrogen Spillover Effect in Electrocatalytic Hydrogen Evolution Process. *Advanced Functional Materials* **2025**, *36*, e28280.

[40] X. Liu, X. Wang, K. Li, J. Tang, J. Zhu, J. Chi, J. Lai, L. Wang. Diluting the Resistance of Built-in Electric Fields in Oxygen Vacancy-Enriched Ru/$NiMoO_{4-x}$ for Enhanced Hydrogen Spillover in Alkaline Seawater Splitting. *Angewandte Chemie International Edition* **2023**, *63*, e202316319

[41] Y. Yang, W. Zheng, P. Wang, Z. Cheng, P. Wang, J. Yang, C. Wang, J. Chen, Y. Qu, D. Wang, *et al*. Tailoring the Hydrogen Spillover Effect in Ni-Based Heterostructure Catalysts for Boosting the Alkaline Hydrogen Oxidation Reaction. *ACS Nano* **2024**, *18*, 24458-24468.

Un-Accepted



Kejun Yan received her master's degree from the University of Science and Technology of China. She is currently pursuing a Ph.D. degree at Southern University of Science and Technology. Her research focuses on electrocatalysts and interfacial processes for the hydrogen evolution reaction in water electrolysis.



Lin Zeng received his bachelor's and master's degrees from Harbin Institute of Technology in 2008 and 2010, respectively, and his Ph.D. degree from the Hong Kong University of Science and Technology in 2014. He is currently a tenured associate professor at Southern University of Science and Technology. His research interests include water electrolysis, fuel cells, and electrochemical energy storage materials and devices.

Just Accepted

Electronic Supplementary Material

Oxide-side lanthanum regulation enables trap-to-relay conversion of hydrogen spillover at MoO_2/Ni_4Mo interfaces

Kejun Yan[1,2], Jiahui Luo[1,2], Baoxin Wu[2,3], Yongbiao Mu[1,2], Zhiqing Tang[1,2], Yu Xu[1,2], Lei Wei[1,2], and Lin Zeng[1,2] (✉)

[1]*Shenzhen Key Laboratory of Hydrogen Energy, Department of Mechanical and Energy Engineering, Southern University of Science and Technology, Shenzhen 518055, China*
[2]*SUSTech Energy Institute for Carbon Neutrality, Southern University of Science and Technology, Shenzhen 518055, China*
[3]*Department of Mechanical Engineering, The Hong Kong Polytechnic University, Hung Hom, Kowloon, Hong Kong SAR, China*

Supporting information to https://doi.org/10.26599/NRE.2026.9120292

Address correspondence to Lin Zeng, zengl3@sustech.edu.cn

1. Experimental Section

1.1 Materials Synthesis

1.1.1 Materials

Potassium hydroxide (KOH, 95%), nickel nitrate ($Ni(NO_3)_2·6H_2O$), ammonium molybdate ($(NH_4)_6Mo_7O_{24}·4H_2O$, lanthanum nitrate hexahydrate ($La(NO_3)_3·6H_2O$), and ethanol were purchased from Macklin Reagent Co. Ltd. Nafion solution (5 wt%) and Fumasep FAA-3-50 membrane for electrochemical tests were bought from Fuel Cell Store (USA). All the chemicals were used directly as received without any further purification. Ultrapure water was used throughout the experiments.

1.1.2 Synthesis of MoO_2/Ni_4Mo Electrocatalysts

About the treatment of nickel foam before use: the nickel foam was immersed in 3 M hydrochloric acid for about 12 minutes, followed by ultrasonic cleaning with deionized water and ethanol for 10 minutes, respectively. The treated nickel foam is then stored and sealed in ethanol.

The MoO_2/Ni_4Mo electrocatalyst was synthesized through a two-step process involving hydrothermal growth of a $NiMoO_4$ precursor followed by rapid reductive Joule heating. Typically, one piece of nickel foam (NF, 2 × 5 cm^2) was immersed in

Just Accepted

60 mL of an aqueous solution containing 4 mmol $Ni(NO_3)_2 \cdot 6H_2O$, 1 mmol $(NH_4)_6Mo_7O_{24} \cdot 4H_2O$. After stirring to obtain a homogeneous solution, the solution together with the NF substrate was transferred into a 100 mL Teflon-lined stainless-steel autoclave and heated at 150 °C for 6 h. After naturally cooling to room temperature, the precursor-loaded NF was collected, thoroughly rinsed with deionized water and ethanol, and dried in a vacuum oven at 60 °C for 12 h. The obtained sample was denoted as $NiMoO_4$.

Subsequently, the $NiMoO_4$/NF precursor was rapidly reduced using a Joule heating system under a flowing mixed gas atmosphere of 10% H_2 and 90% Ar with a total flow rate of 200 sccm. The Joule heating current was carefully controlled to raise the temperature to approximately 500 °C within 1 s, maintained for 300 s, and then rapidly cooled to room temperature. The final product was denoted as MoO_2/Ni_4Mo.

1.1.3 Synthesis of x%La-MoO_2/Ni_4Mo Electrocatalysts

The *x*%La-MoO_2/Ni_4Mo electrocatalysts were synthesized through the same precursor-to-heterostructure conversion process, except that different amounts of $La(NO_3)_3 \cdot 6H_2O$ were introduced during the hydrothermal precursor-growth step. Typically, one piece of nickel foam (NF, 2 × 5 cm^2) was immersed in 60 mL of an aqueous solution containing 4 mmol $Ni(NO_3)_2 \cdot 6H_2O$, 1 mmol $(NH_4)_6Mo_7O_{24} \cdot 4H_2O$, and a certain amount of $La(NO_3)_3 \cdot 6H_2O$. Specifically, 0.05, 0.10, 0.25, and 0.50 mmol $La(NO_3)_3 \cdot 6H_2O$ were added to prepare 1%La-, 2%La-, 5%La-, and 10%La-$NiMoO_4$ precursors, respectively. After stirring to form a homogeneous solution, the solution and NF substrate were transferred into a 100 mL Teflon-lined stainless-steel autoclave and heated at 150 °C for 6 h. After naturally cooling to room temperature, the obtained precursor-loaded NF was thoroughly washed with deionized water and ethanol, and then dried in a vacuum oven at 60 °C for 12 h.

The as-prepared *x*%La-$NiMoO_4$ precursor was then subjected to rapid reductive Joule heating under a mixed gas flow of 10% H_2 and 90% Ar with a total flow rate of 200 sccm. The temperature was rapidly increased to approximately 500 °C within 1 s, held for 300 s, and then quickly cooled to room temperature. The final products were denoted as *x*%La-MoO_2/Ni_4Mo. Unless otherwise stated, La-MoO_2/Ni_4Mo refers to the optimized 2%La-MoO_2/Ni_4Mo sample, which was prepared by adding 0.1 mmol $La(NO_3)_3 \cdot 6H_2O$ to the precursor solution. Here, *x*% denotes the nominal La precursor

Just Accepted

content used for sample labeling, defined as the molar ratio of $La(NO_3)_3 \cdot 6H_2O$ to the total amount of Ni and Mo precursor salts, rather than the actual La atomic percentage in the final catalyst.

$$x = \frac{n\left(\mathrm{La}\left(\mathrm{NO_3}\right)_3 \cdot 6\mathrm{H_2O}\right)}{n\left(\left(\mathrm{NH_4}\right)_6 \mathrm{Mo_7O_{24}} \cdot 4\mathrm{H_2O}\right) + n\left(\mathrm{Ni}\left(\mathrm{NO_3}\right)_2 \cdot 6\mathrm{H_2O}\right)} \quad (1)$$

1.2 Characterizations

X-ray diffraction (XRD) patterns were collected over the 2θ range 5-90º and a scan rate of 0.02 degrees/second on Bruker Advance D8 with Cu Ka radiation (λ=0.15416 nm). Raman spectra were collected on LabRAM HR Evolution in Via Reflex spectrometer system equipped with a 532 nm laser excitation source. Scanning electron microscopy (SEM) images were acquired using a ZEISS Sigma 300 with an accelerating voltage of 5 kV. A Talos F200X G2 was used to obtain the transmission electron microscopy (TEM) images. The TEM images were acquired at 200 kV with the samples deposited on a holey carbon film-covered copper grid. High-resolution transmission electron microscopy (HR-TEM) was conducted using a Titan Themis G2 double spherical aberration-corrected transmission electron microscope with a 300 kV accelerating voltage. X-ray photoelectron spectra (XPS, Escalab 250Xi) were acquired on a Thermo SCIENTIFIC ESCALAB 250Xi with Al Kα ($h\upsilon$ = 1486.8 eV) as the excitation source.

Ni and Mo K-edge X-ray absorption near-edge structure (XANES) and extended X-ray absorption fine structure (EXAFS) data were obtained at beamline 8 of the Synchrotron Light Research Institute (SLRI), Nakhon Ratchasima, Thailand. Powder samples were homogeneously mixed with cellulose to obtain a metal concentration around 1000 ppm. A Si (111) single crystal was used to monochromatize the X-ray beam. The raw X-ray absorption fine structure (XAFS) data were processed (background-subtraction, normalization, and Fourier transformation) using standard procedures within the Athena module of the IFEFFIT software package. EXAFS fitting was performed by the Artemis module, following the EXAFS equation below:

$$\chi(k) = \sum_j \frac{N_j S_0^2 F_j(k)}{kR_j^2} \exp\left[-2k^2\sigma_j^2\right] \exp\left[\frac{-2R_j}{\lambda(k)}\right] \sin\left[2kR_j + \phi_j(k)\right] \quad (2)$$

where S_0^2 is the amplitude reduction factor, $F_j(k)$ is the effective curved-wave

Just Accepted

backscattering amplitude, N_j is the number of neighbors in the j_{th} atomic shell, R_j is the distance between the X-ray absorbing central atom and the atoms in the j_{th} atomic shell, λ is the mean free path in Å, $\phi_j(k)$ is the phase shift, σ_j^2 is the Debye-Waller parameter of the j_{th} atomic shell (variation of distances around the average R_j).

The wavelet transform was processed by Morlet wavelet using the software of Web-WTexafs. The complex Morlet wavelet is shown in the following equation:

$$\Psi(t) = \frac{1}{\sqrt{2\pi}\sigma}\left(e^{i\eta t} - e^{-\eta^2\sigma^2/2}\right)e^{-t^2/\left(2\sigma^2\right)} \quad (3)$$

the parameter σ is the half-width of the Gaussian envelope, and the parameter η determines the oscillations of the wave. The real constant $-e^{-\eta^2\sigma^2/2}$ ensures the wavelet function with zero mean.

The parameter σ and η were set as 3 and 2, respectively, for the wavelet transform of each sample in this work. The *k*-space data of each sample with exact *k* range of 0-15 $Å^{-1}$ and *R* range of 1-4 Å for Fourier transformation was processed with the script, generating a matrix containing the continuous transform data.

1.3 Electrochemical hydrogen evolution mechanism

The alkaline hydrogen evolution reaction (HER) involves three elementary steps: the Volmer, Tafel, and Heyrovsky steps, which are described by Eqs. (4)-(6), respectively. In Eqs. (4) - (6), cat. denotes a catalyst site and H* denotes hydrogen intermediate.

$$H_2O + e^- + \text{cat.} \rightarrow H^*\text{-cat} + OH^- \quad (4)$$

$$2H^*\text{-cat} \rightarrow H_2\uparrow \quad (5)$$

$$H^* - \text{cat} + H_2O + e^- \rightarrow \text{cat.} + OH^- + H_2\uparrow \quad (6)$$

1.4 Electrochemical measurements

The electrocatalytic activity was evaluated on IviumStat systems equipped with a three-electrode cell. All the measurements were performed at room temperature in a 1 M KOH alkaline solution. The as-obtained electrodes were used as the working electrode. The Pt/C ink was prepared by mixing 495 μL of deionized water, 495 μL of isopropanol, and 10 μL of Nafion solution. The ink was deposited onto nickel foam

Just Accepted

(NF) to give a Pt/C catalyst loading of 0.5 mg cm^{-2}. The Pt/C electrode was tested under the same HER conditions as La-MoO_2/Ni_4Mo. A graphite rod was used as the counter electrode and an Hg/HgO electrode was used as the reference electrode. The Hg/HgO electrode was calibrated using bubbling H_2 gas on a Pt coil electrode. The linear sweep voltammetry curves and cyclic voltammetry curves were recorded at a scan rate of 5 mV s^{-1}. The polarization curves towards HER were obtained by linear sweep voltammetry from 0.1 to -0.4 V with a sweep rate of 5 mV s^{-1}. Potentials in this work were all referred to the reversible hydrogen electrode (RHE) through the Nernst equation as follows: E (vs RHE) = E (vs.Hg/HgO) + 0.099 + 0.0591 × pH. The HER polarization curves were corrected during data processing using 80% iR compensation: $E_{corrected} = E_{measured} - 0.80iR_u$, with the current sign convention taken into account. Unless otherwise specified, reported HER overpotentials are based on the iR-corrected polarization curves. Electrochemical impedance spectroscopy (EIS) was performed from 0.01 Hz to 100 kHz. The electrochemically active surface areas (ECSA) were studied based on the electrochemical double-layer capacitance of various electrocatalysts at non-faradaic overpotentials. By plotting the difference of current density (J) between the anodic and cathodic sweeps ($J_{anodic} - J_{cathodic}$) at 0.1 V vs. RHE against the scan rates of 60, 80, 100, 120, and 140 mV s^{-1}, a linear trend was observed. The slope of the fitting line is equal to twice the geometric double layer capacitance (C_{dl}). Namely, $C_{dl} = (J_{anodic} - J_{cathodic})/2$. The durability test was conducted in galvanostatic mode at -10 mA cm^{-2} in 1.0 M KOH solution at room temperature.

1.5 Anion-exchange-membrane water electrolyzer (AEMWE) setup

The AEMWE comprises the anode, cathode, gas diffusion layer, and anion exchange membrane (Fumasep FAA-3-50). The as-obtained electrodes as the cathode electrocatalyst. The selected anode material is 1 cm^2 NiFe layered double hydroxide (NiFe-LDH) with a loading capacity of 1 mg/cm^2. The preparation method is the same as that described in the reference[1]. Before use, the anion exchange membrane (1.5 × 1.5 cm^2) was placed in 1 M KOH for 24 h, and the active working electrode area was 1 cm^2 in the single-cell. The alkaline electrolyte (1 M KOH) was recycled into the cathode and anode side through a self-priming pump from the electrolyte reservoir. The electrolyzer was heated by a heating rod, and an automatic temperature control

Just Accepted

device precisely controlled the temperature. When the temperature of the cell was stabilized, the performance of the cell was analyzed. In this work, all electrochemical testing was performed on the single-cell. The polarization curves of the AEM single-cell were evaluated with a scan rate of 5 mV s^{-1} by the MultiStat workstation without *iR* compensation. The stability of AEM water electrolyzer systems was evaluated with the Neware electrochemical station.

1.6 Theoretical Calculations

First-principle calculations. All the density functional theory (DFT) calculations are performed by the Vienna Ab initio Simulation Package (VASP)[2] with the projector augmented wave (PAW) method. The exchange-functional is treated using the generalized gradient approximation (GGA) with Perdew-Burke-Ernzerhof (PBE) functional[3-5]. The energy cutoff for the plane wave basis expansion was set to 400 eV. Partial occupancies of the Kohn-Sham orbitals were allowed using the Gaussian smearing method and a width of 0.2 eV. The self-consistent calculations apply a convergence energy threshold of 10-5 eV, and the force convergency was set to 0.05 eV/Å. The free energy corrections were considered at the temperature of 298 K, following:

$$\Delta G = \Delta E + \Delta G_{\mathrm{ZPE}} + \Delta G_{\mathrm{U}} - T\Delta S \tag{7}$$

where ΔE, ΔG_{ZPE}, ΔG_{U}, and ΔS refer to the DFT calculated energy change, the correction from zero-point energy, the correction from inner energy, and the correction from entropy. The reaction free energy of relevant steps was calculated following the computational hydrogen electrode (CHE) model.

Just Accepted

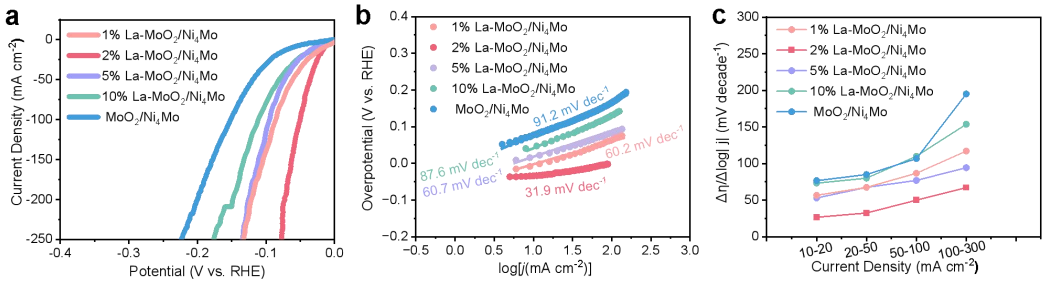


Figure S1. Optimization of nominal La precursor content in *x*%La-MoO_2/Ni_4Mo. (a) HER polarization curves. (b) Tafel plots. (c) The ratio of $\Delta\eta/\Delta\log|j|$ at different current densities.

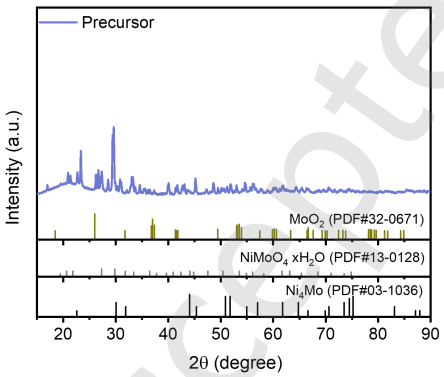


Figure S2. XRD patterns of the precursor.

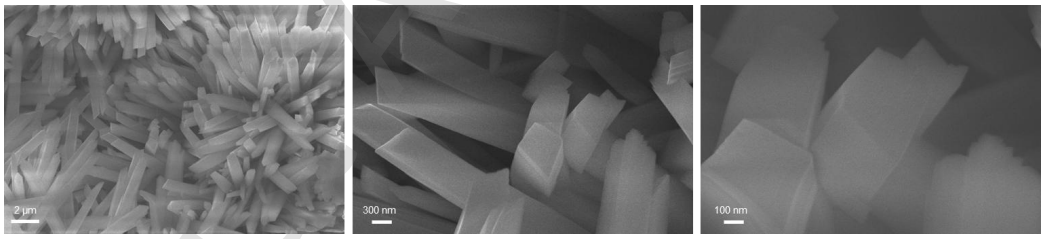


Figure S3. SEM of the precursor.

Just Accepted

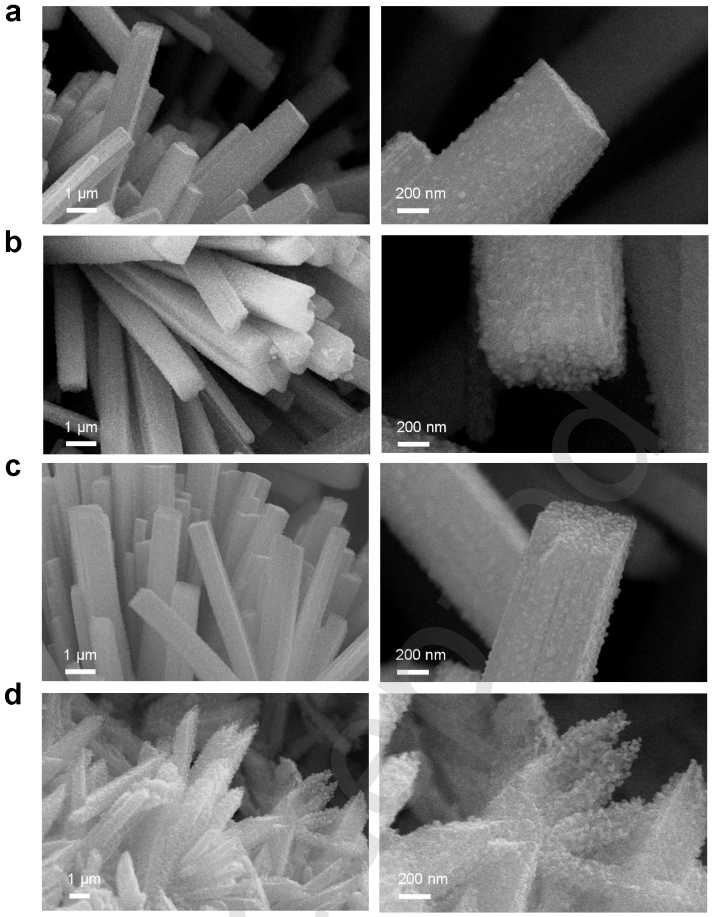


Figure S4. SEM of *x*%La-MoO_2/Ni_4Mo. (a) MoO_2/Ni_4Mo. (b) 1%La-MoO_2/Ni_4Mo. (c) 5%La-MoO_2/Ni_4Mo. (d) 10%La-MoO_2/Ni_4Mo.

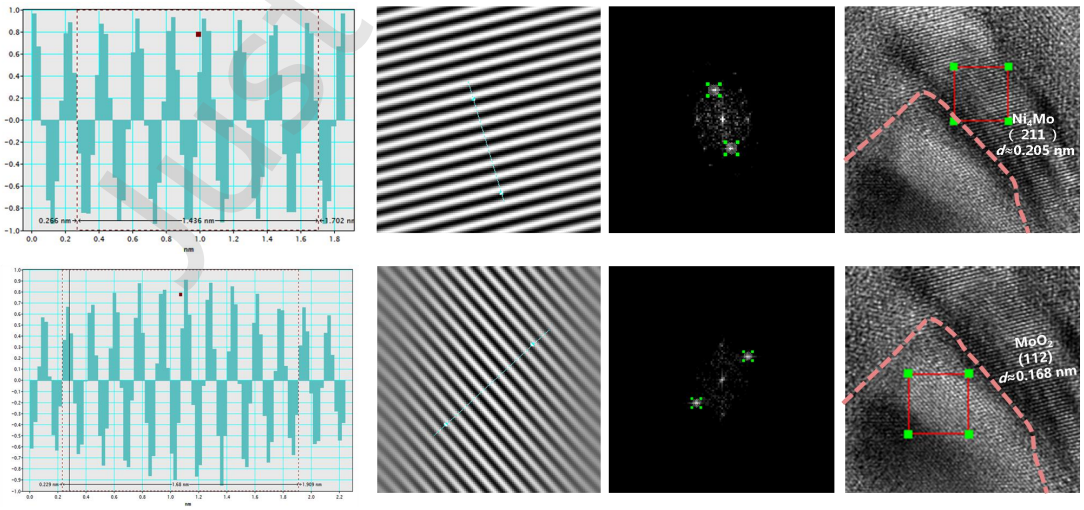


Figure S5. HRTEM of MoO_2/Ni_4Mo.

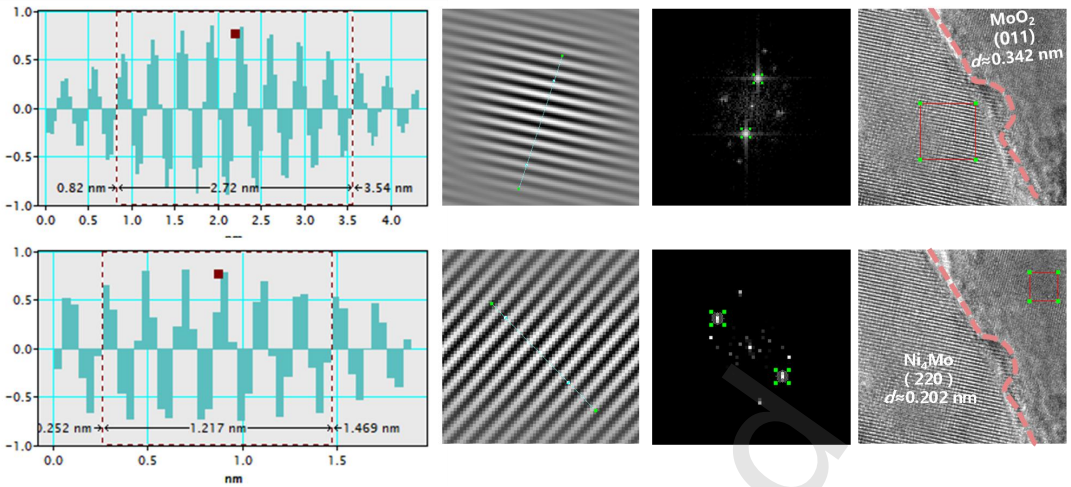


Figure S6. HRTEM of La-MoO_2/Ni_4Mo.

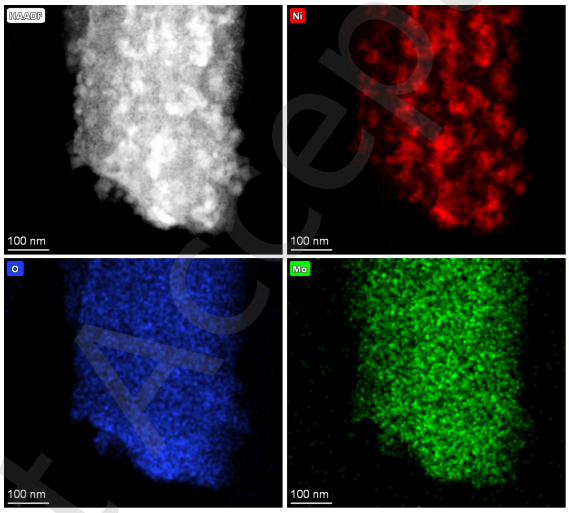


Figure S7. Elemental mapping images of MoO_2/Ni_4Mo.

Note: It can be clearly seen that Ni is concentrated in the particles on the surface of the rods.

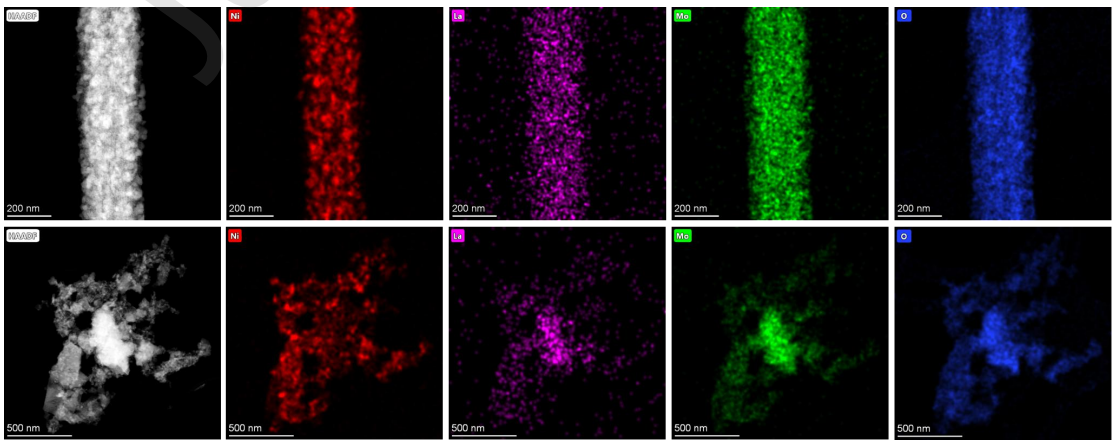


Figure S8. Elemental mapping images of La-MoO_2/Ni_4Mo.

Just Accepted

Note: The catalyst fragments after ultrasonic treatment can clearly show that lanthanum is enriched in the oxide.

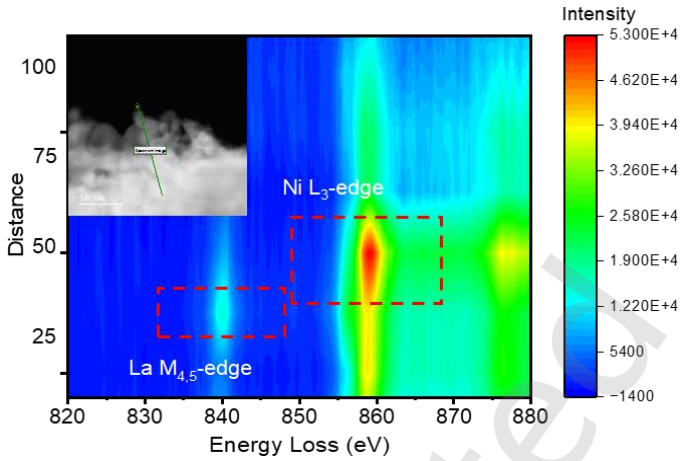


Figure S9. AC-EELS maps of La-MoO_2/Ni_4Mo with La $M_{4,5}$-edge and Ni L_3-edge.

Note: The line sweep of spherical aberration eels clearly shows that La and Ni do not appear and disappear simultaneously; they are distributed over different intervals.

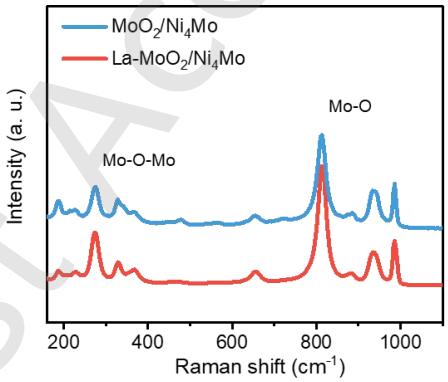


Figure S10. Raman of MoO_2/Ni_4Mo and La-MoO_2/Ni_4Mo.

Just Accepted

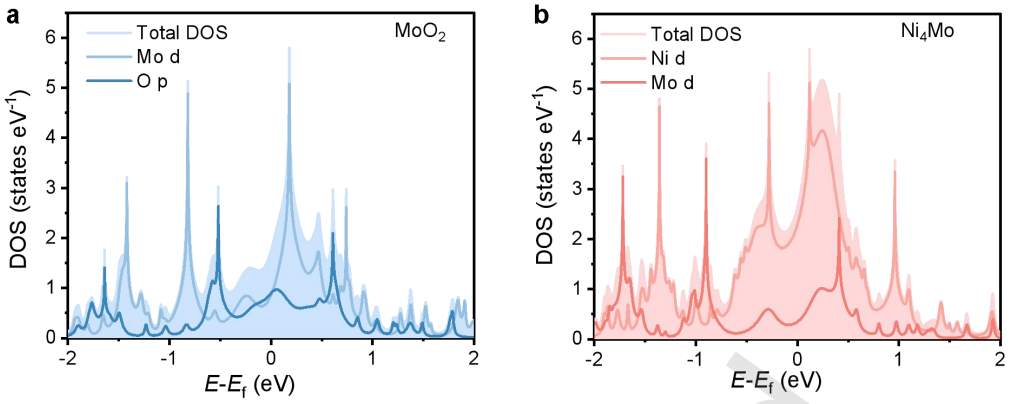


Figure S11. Element and orbital-projected DOS of the interfacial layer. (a) MoO_2. (b) Ni_4Mo.

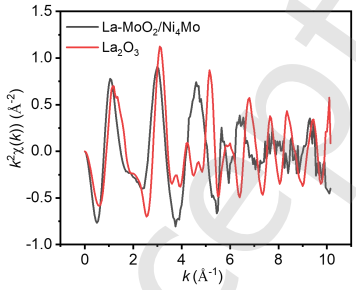


Figure S12. La L_3-edge *k*-space EXAFS fitting.

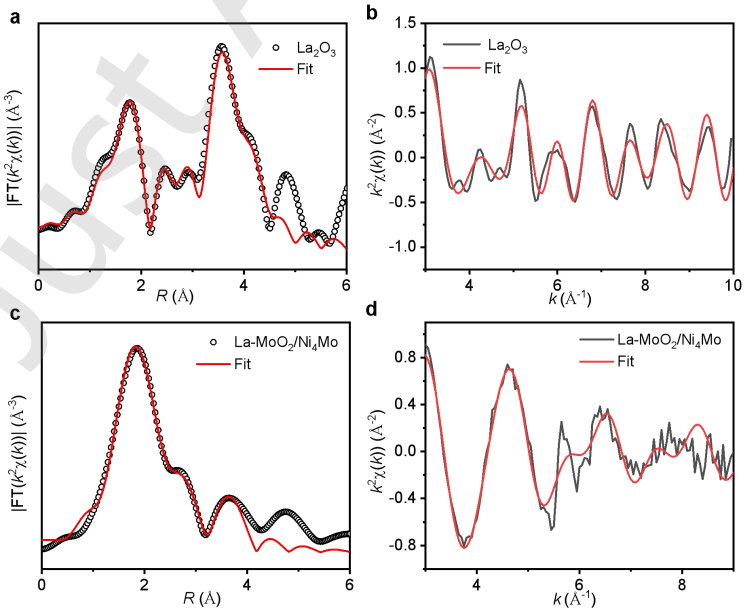


Figure S13. FT-EXAFS fitting for the La_2O_3 and La-MoO_2/Ni_4Mo.

Just Accepted

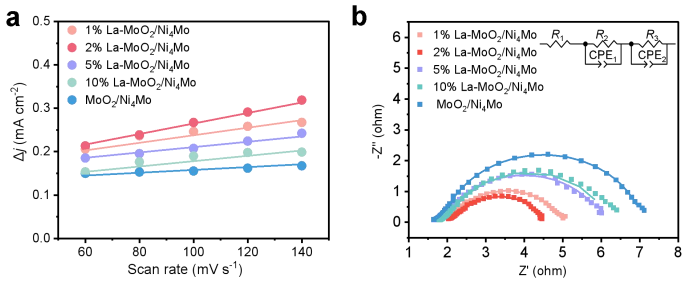


Figure S14. (a) C_{dl} of *x*%La-MoO_2/Ni_4Mo. (b) EIS of *x*%La-MoO_2/Ni_4Mo.

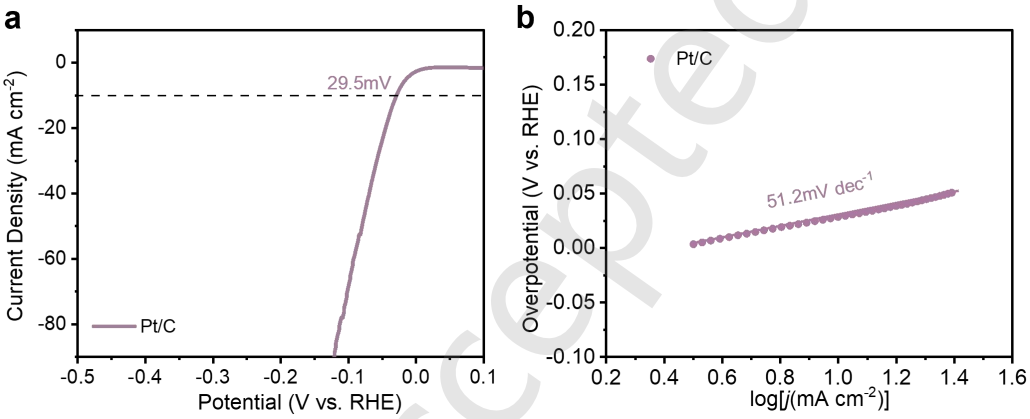


Figure S15. (a) Polarization curve of commercial Pt/C in 1.0 M KOH. (b) Corresponding Tafel plot.

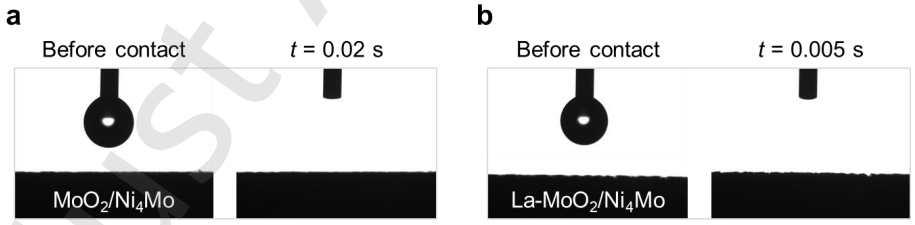


Figure S16. Water contact-angle measurements for (a) MoO_2/Ni_4Mo and (b) La-MoO_2/Ni_4Mo.

Just Accepted

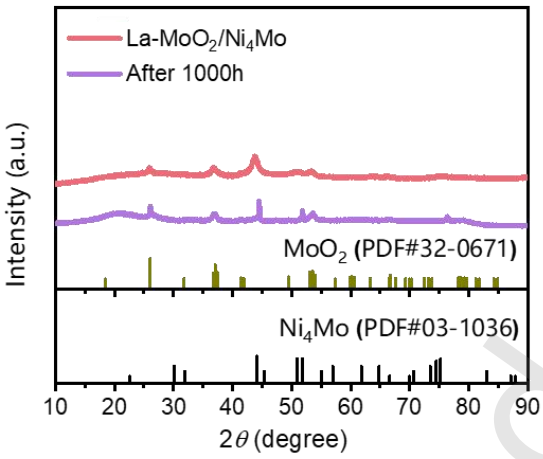


Figure S17. XRD patterns of La-MoO_2/Ni_4Mo before and after 1000 h of AEMWE operation.

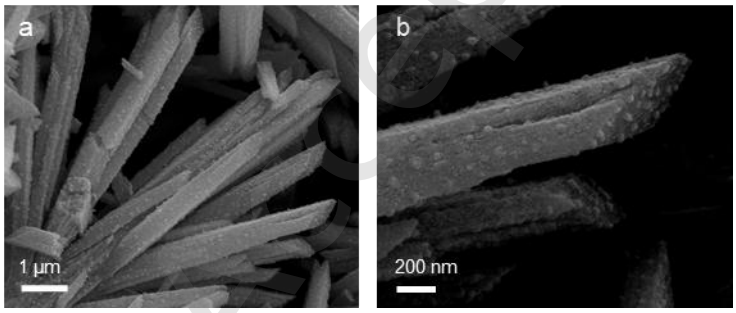


Figure S18. SEM images of La-MoO_2/Ni_4Mo after 1000 h of AEMWE operation. (a) low-magnification image. (b) high-magnification image.

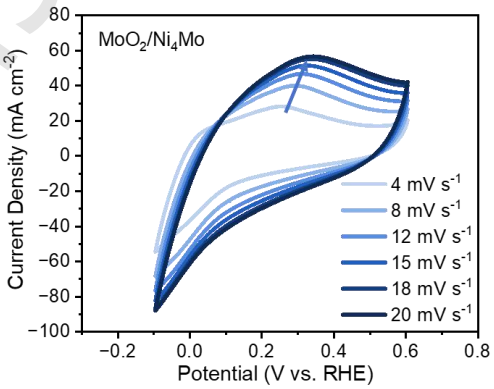


Figure S19. Scan-rate-dependent cyclic voltammetry of MoO_2/Ni_4Mo.

Just Accepted

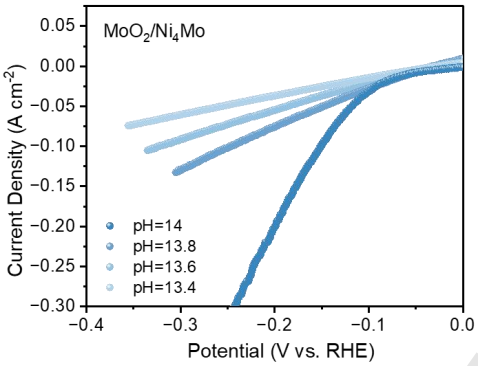


Figure S20. pH-dependent HER kinetics of MoO_2/Ni_4Mo.

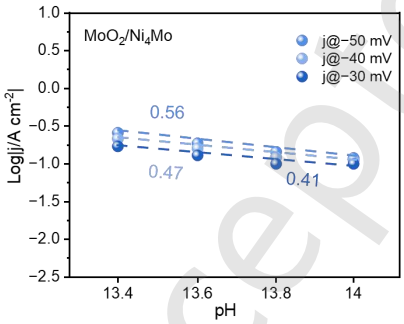


Figure S21. The corresponding reaction-order analysis of MoO_2/Ni_4Mo with pH.

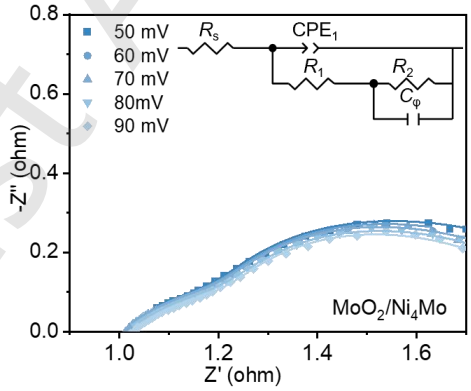


Figure S22. Representative operando EIS spectra and equivalent circuit containing the H*-adsorption/transfer-related (R_2-C_φ) branch of MoO_2/Ni_4Mo.

Just Accepted

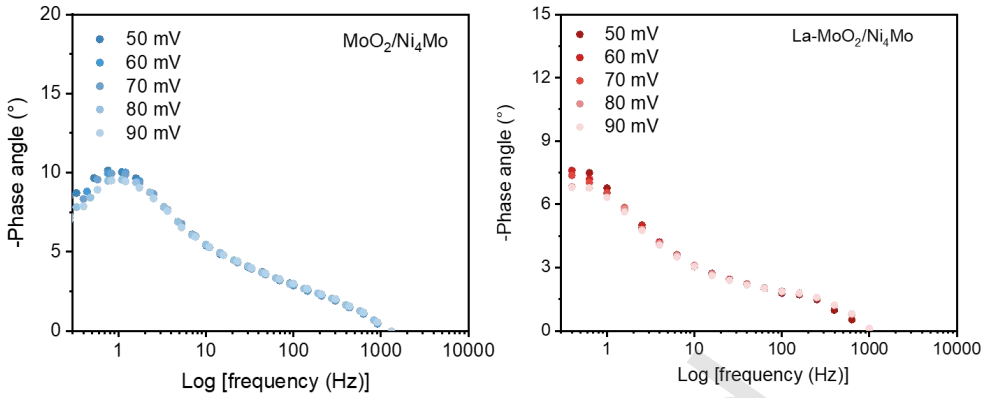


Figure S23. Phase angles of MoO_2/Ni_4Mo and La-MoO_2/Ni_4Mo.

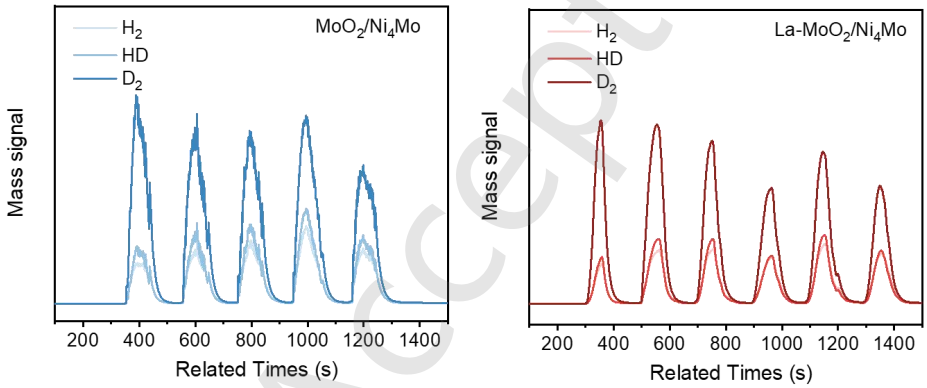


Figure S24. Operando DEMS isotope-output distribution in 1M KOD/D_2O.

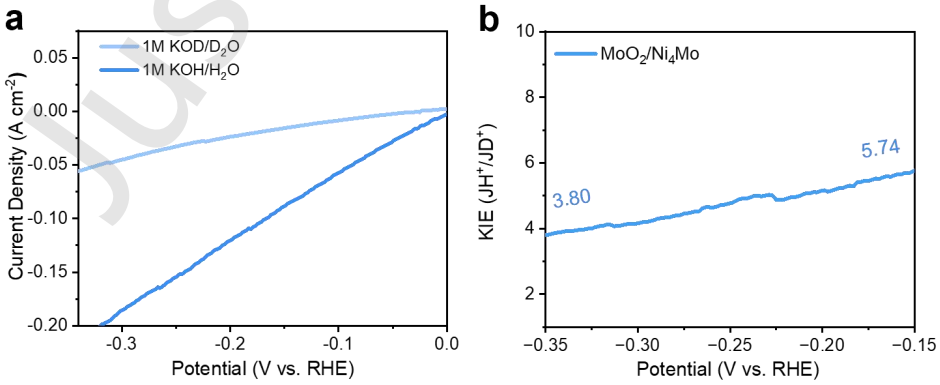


Figure S25. (a) Isotope polarization curves in H_2O/KOH and D_2O/KOD. (b) The corresponding KIE values.

Just Accepted

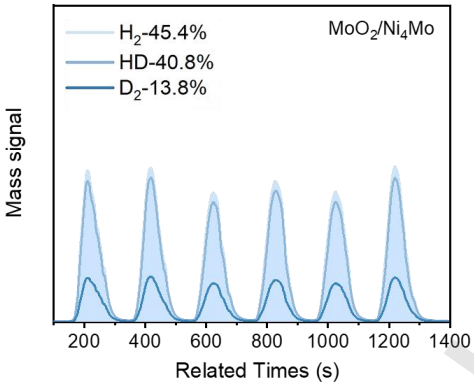


Figure S26. Operando DEMS isotope-output profiles and normalized ion-current contributions of H_2, HD, and D_2 over MoO_2/Ni_4Mo in mixed H_2O/D_2O electrolyte.

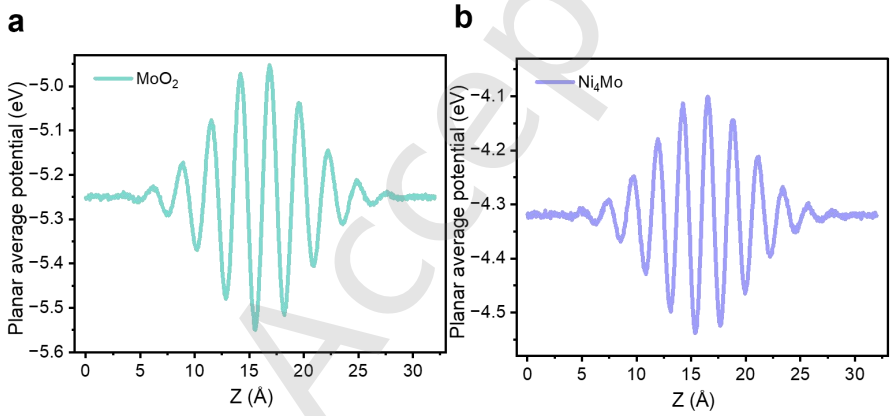


Figure S27. Planar-averaged electrostatic-potential profiles. (a) MoO_2. (b) Ni_4Mo.

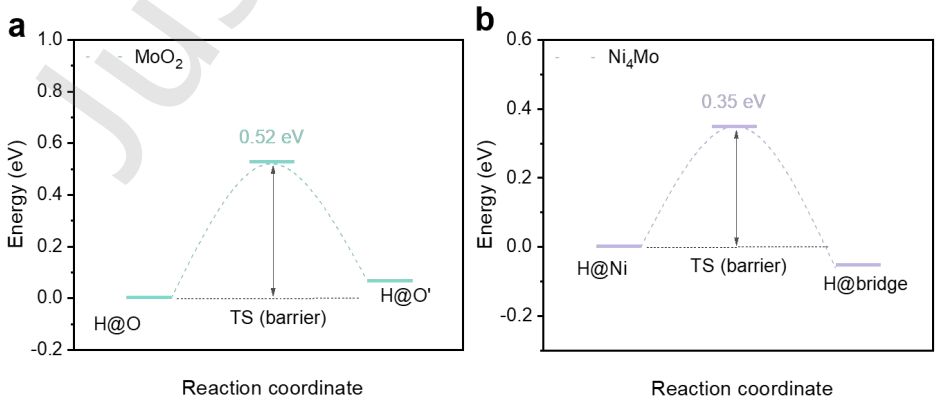


Figure S28. The barrier of interfacial H* transfer. (a) MoO_2. (b) Ni_4Mo.

Just Accepted

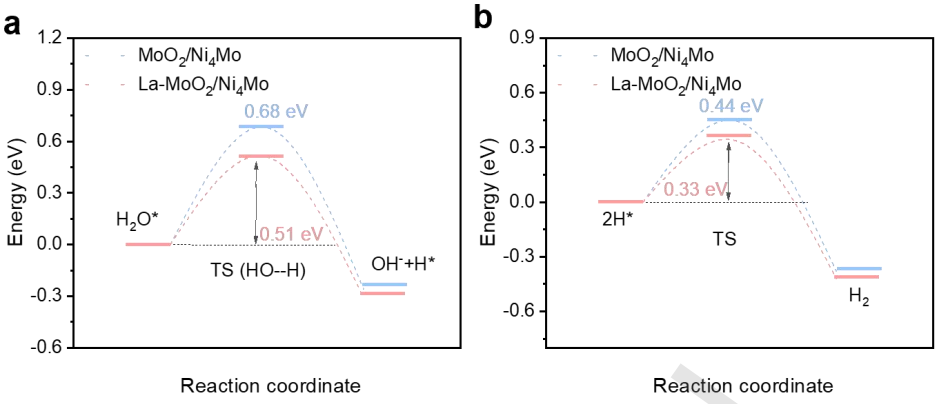


Figure S29. The barrier of water dissociation and H_2 release

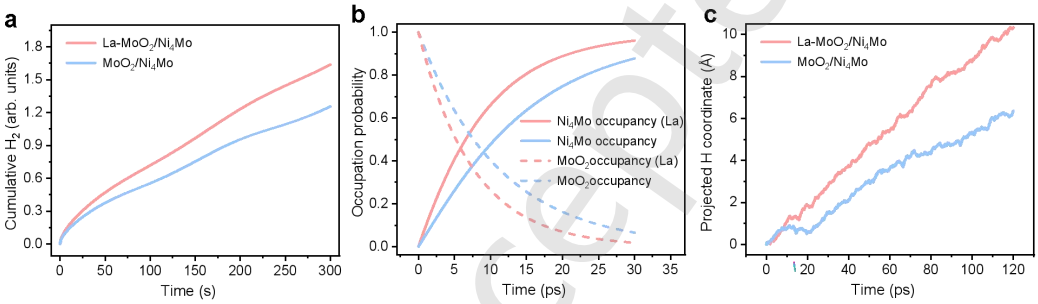


Figure S30. H* transfer kinetics.

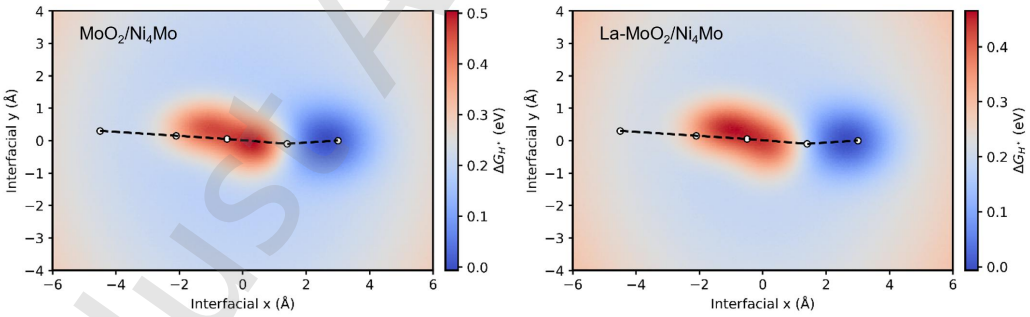


Figure S31. 2D landscape.

Table S1. ICP-OES-quantified Ni, Mo, and La contents of *x*%La-MoO_2/Ni_4Mo catalysts.

Sample	Ni (wt.%)	Mo (wt.%)	La (wt.%)
MoO_2/Ni_4Mo	**32.9**	**51.2**	/
1%La-MoO_2/Ni_4Mo	32.85	50.8	0.78
2%La-MoO_2/Ni_4Mo	32.2	50.7	1.81

Just Accepted

5%La-MoO_2/Ni_4Mo	30.89	52.67	4.56
10%La-MoO_2/Ni_4Mo	29.04	48.94	8.92

Table S2. Quantitative DOS descriptors derived from layer-and orbital-resolved DOS calculations for pristine and La-regulated MoO_2/Ni_4Mo interfacial models.

Sample	Total DOS at E_f/states eV^{-1}	Surface/interfacial DOS at E_f/states eV^{-1}	Dominant frontier orbitals
MoO_2/Ni_4Mo	43.5	15.2	Ni-d/Mo-d
La-MoO_2/Ni_4Mo	28.6	6	Ni-d/Mo-d

Table S3. EXAFS fitting parameters at the La L3-edge for various samples (S_0^2=1.0 from La_2O_3).

Sample	Shell	*CN*[a]	*R*[b](Å)	σ^{2c}(Å^2)	ΔE_0[d](eV)	*R* factor
La_2O_3	La-O	4	2.36 ± 0.02	0.0157	2.7 ± 1.6	0.0092
	La-O	3	2.84 ± 0.03	0.0113	1.1 ± 1.4	
	La-La	6	3.87 ± 0.03	0.0059	11.5 ± 1.8	
	La-La	6	4.52 ± 0.06	0.0153	11.8 ± 3.5	
La-MoO_2/Ni_4Mo	La-O	3.9 ± 0.3	2.39 ± 0.01	0.0070	-6.6 ± 0.7	0.0115
	La-O	1.8 ± 0.3	2.72 ± 0.02	0.0076	9.3 ± 1.3	
	La-M	3.7 ± 0.7	3.87 ± 0.02	0.0130	1.0 ± 1.2	

[a]*CN*: coordination numbers; [b]*R*: bond distance; [c]σ^2: Debye-Waller factors; [d] ΔE_0: the inner potential correction. *R* factor: goodness of fit. A reasonable range of EXAFS fitting parameters: $0.70 < S_0^2 < 1.00$; CN > 0; $\sigma^2 > 0$ Å^2; $|\Delta E_0| < 15$ eV; *R* factor < 0.02.

The obtained XAFS data were processed in Athena (version 0.9.26) [J. Synchrotron Rad. 2005, 12, 537] for background, pre-edge line, and post-edge line calibrations. Then Fourier transformed fitting was carried out in Artemis (version 0.9.26) [J. Synchrotron Rad. 2005, 12, 537]. The k^3 weighting, *k*-range of 3 - 9.0 Å^{-1} and *R* range of 1 - 4.5 Å were used for the fitting of La_2O_3; The k^3 weighting, *k*-range

Just Accepted

of 3 - 8.0 $Å^{-1}$ and *R* range of 1 - 4.0 Å were used for the fitting of the sample.

Table S4. Operando EIS fitting parameters of MoO_2/Ni_4Mo at different overpotentials.

Overpotential/mV	*R*s/Ω	CPE-T	CPE-P	R_1/Ω	R_2/Ω	C_φ
50 mV	1.008	0.408	0.502	0.519	0.608	0.170
60 mV	1.009	0.372	0.508	0.507	0.573	0.171
70 mV	1.006	0.352	0.510	0.500	0.543	0.172
80 mV	1.015	0.348	0.515	0.496	0.522	0.176
90 mV	1.018	0.319	0.520	0.466	0.514	0.177

Just Accepted

Table S5. Operando EIS fitting parameters of La-MoO_2/Ni_4Mo at different overpotentials.

Overpotential/mV	*R*s/Ω	CPE-T	CPE-P	R_1/Ω	R_2/Ω	C_φ
50 mV	0.963	1.354	0.333	0.677	1.007	0.210
60 mV	0.969	1.272	0.338	0.602	0.855	0.234
70 mV	0.967	1.207	0.347	0.569	0.665	0.277
80 mV	0.973	1.072	0.367	0.463	0.540	0.314
90 mV	0.979	0.960	0.380	0.400	0.467	0.375

Just Accepted

Table S6. Background-corrected integrated DEMS peak areas of H_2, HD, and D_2 at m/z = 2, 3, and 4 in mixed H_2O/D_2O electrolyte

Sample	A_{H2} at m/z = 2/a.u.	A_{HD} at m/z = 3/a.u.	A_{D2} at m/z = 4/a.u.
MoO_2/Ni_4Mo	1.06×10^{-5}	9.54×10^{-6}	3.22×10^{-6}
La-MoO_2/Ni_4Mo	1.24×10^{-5}	2.00×10^{-5}	9.72×10^{-6}

Note: A_{H2}, A_{HD}, and A_{D2} were obtained by integrating the background-corrected (m/z = 2), 3, and 4 ion-current signals over the selected response region.

Just Accepted

Table S7. Normalized DEMS ion-current contributions of H_2, HD, and D_2 derived from the background-corrected integrated peak areas.

Sample	H_2 contribution/%	HD contribution/%	D_2 contribution/%
MoO_2/Ni_4Mo	45.4	40.8	13.8
La-MoO_2/Ni_4Mo	29.4	47.6	23.1

Note: The normalized DEMS ion-current contribution was calculated as：

$x = \frac{A_i}{A_{H2}+A_{HD}+A_{D2}} \times 100\%$, where A_i represents the background-corrected integrated peak area of each isotope-related signal. The values represent relative DEMS ion-current contributions rather than absolute molar gas fractions.

Just Accepted

Table S8. The HER activity (Overpotential at 10 mA cm^{-2} and Tafel slope) comparison between our work and other electrocatalysts in 1 M KOH.

Sample	Overpotential (mV)	Tafel slope (mV dec^{-1})	Reference
This work	14	31.9	/
MoO_2-Ni NWs	58.4	36.6	ACS Catal. 2019, 9, 2275-2285
MoO_2/Ni@NF	50.5	65.52	ACS Appl. Mater. Interfaces 2021, 13, 39470-39479
Ni-Mo@ACF	87	107	ACS Appl. Energy Mater. 2023, 6, 11, 5787-5796
Ni/NiFeMoO_x/NF	22	76	Adv. Sci. 2020, 7, 1902034
Ni/MoO_{2-x}/NF	27	26	Chem. Eng. J., 2023, 464
Mo-NiO/Ni	50	86	ACS Energy Lett. 2019, 4, 3002-3010
Ni-NiO/$Ti_3C_2T_x$	72	55.4	ACS Appl. Mater. Interfaces 2022, 14, 47529-47541
Ni-CeF_3-VN	33	37.1	Adv. Funct. Mater. 2021, 31, 2104827
W_2C-Ni/CC	37	64.3	Appl. Surf. Sci. 2023, 630.
NiFeCoS$_x$@$FeNi_3$	88	116	J. Mater. Chem. A, 2022, 10, 5442
Ni-Co alloy	54	26	Appl. Surf. Sci., 2021, 539
Ru@Ni-MOF	22	40	Angew. Chem. Int. Ed. 2021, 60, 22276-22282

Just Accepted

Table S9. Overall water-splitting performance of different water electrolyzers. The cell voltages at 500 and 1000 mA cm^{-2} are denoted as V_{500} and V_{1000}.

Sample	V_{500} (V)	V_{1000} (V)	Reference
This work	1.63	1.74	/
Raney NiMo‖$Ni(OH)_2$-Fe	1.7	1.85	ACS Appl. Energy Mater. 5, 2221-2230 (2022)
PtRu/C‖IrO_2	1.8	1.95	Nat. Energy 5, 378-385 (2020)
Ru-Co_3O_4‖Ru-Co_3O_4		2.03	Appl. Catal., B 343, 123578 (2024).
$MoNi_4/MoO_2$‖Ni_2P@$FePO_x$	1.75	1.84	Appl. Catal. B: Environ. 306, 121127 (2022)
NA-Ru_3Ni/C‖NA-Ru_3Ni/C		2.05	Energy Environ. Sci. 16, 285-294 (2023)
Ni-MoNSSM‖Ni-MoNSSM	1.71	1.78	Adv. Mater. 2022, 34, 2201774
Pt-$MoAl_{1-x}B$‖RuO_2	1.85	2	Energy Environ. Sci., 2023, 16, 4093-4104
MoO_2@Ru‖NiFe LDH	1.66	1.78	Adv. Energy Mater. 2023, 13, 2301492
RuMo/Cu_2O@C‖NiFe LDH	1.7	1.78	Adv. Mater. 2025, 37, 2416658.
$MoO_2/MoNi_4$‖HS-RuCo/NC	1.8	2.07	Small, 2023. 19(28): p. e2207611.
$NiFe_2O_4$‖Ni_3N/Ni	1.88		Energy Environ. Sci. 15, 185-195 (2022)
RuO_2/NiFe‖P-Os/NiFe	1.86	2.02	Adv. Funct. Mater. n/a, 2408517 (2024)
u/P-MoB/NF ‖ RuO_2/NF	1.71	1.78	Adv. Energy Mater. 2024, 14, 2303384

Just Accepted

Reference:

[1] B. Wu, Z. Zhang, Y. Hu, J. Liu, X. Zou, Q. Zhang, K. Yan, S. Xi, G. Wang, X. Zhang, L. Zeng, L. An, *Chem. Eng. J.* **2024**, *495*.
[2] G. Kresse, J. Furrbmiiller, *Comp. Mater. Sci.* **1996**, *6*, 15-50.
[3] G. Kresse, D. Joubert, *Phys. Rev. B* **1999**, *59*, 1758.
[4] J. P. Perdew, K. Burke, M. Ernzerhof, *Phys. Rev. Lett.* **1996**, *77*, 3865-3868.
[5] G. Kresse, J. Furthmuller, *Phys. Rev. B* **1994**, *50*, 17953-17979.

Just Accepted